Physics of the Earth and Planetary Interiors 310 (2021) 106630

Contents lists available at ScienceDirect

Physics of the Earth and Planetary Interiors

journal homepage: www.elsevier.com/locate/pepi

Heat diffusion in numerically shocked ordinary chondrites and its contribution to shock melting

Juulia-Gabrielle Moreau [a,b,*], Sabrina Schwinger [c]

[a] Department of Geosciences and Geography, University of Helsinki, Finland
[b] Institute of Ecology and Earth Sciences, Department of Geology, University of Tartu, Estonia
[c] German Aerospace Center (DLR), Berlin, Germany

ARTICLE INFO

Keywords:
Ordinary chondrites
Shock metamorphism
Heat diffusion
Shock-darkening
iSALE

ABSTRACT

High pressure shock metamorphism in ordinary chondrites involves heating and melting of individual phases from shock entropy, pore collapse, frictional heating, and heat transfer. Numerical models using shock physics codes have recently been used to comprehend the mechanism of shock heating and melting in multiphase mesoscale models. Such models suggest that the formation of sulfide and metal melt veins in ordinary chondrites (shock-darkening) can be explained by preferential heating and melting of iron and iron sulfides during shock. However, those models usually dismissed heat transfer between heterogeneously shock heated phases. This leads to an underestimation of the degree of melting in phases that experienced low degrees of shock heating (e.g. iron metal) but are in direct contact with strongly shock heated phases (e.g. iron sulfides). In our study, we implemented a finite difference 2-D heat diffusion code to model heat diffusion among neighboring grains in shock heated multiphase meshes that represent typical textural relations of silicate, sulfide and metal grains in ordinary chondrites. Post-shock temperature maps for each textural model were calculated using the iSALE shock physics code and used as input for the diffusion code. We find that heat diffusion, not initial shock heating, is the principal cause for heating and melting of metals in eutectic contact with iron sulfides at ~50 GPa of pressure. In addition we study the effects of iron and troilite grain sizes, shock pressures and pre-shock porosities of the silicate matrix, and discuss the preservation of melt allowing melt migration in shock-darkened meteorites and the observation of metal-silicate intermixed melting. With our work, we demonstrate that the consideration of heat diffusion during and after shock is crucial for a better understanding of melting features in both experimentally and naturally shocked ordinary chondrites.

1. Introduction

Shock metamorphism in ordinary chondrites is associated with impact processes between asteroids (Stöffler et al., 1991, 2018; Fritz et al., 2017) inducing fracturing, crystal and lattice deformation, heating, melting, and phase changes under shock compression. Fracturing and crystal/lattice deformation are more characteristic of low shock stages (C—S1 to C—S4, <35 GPa, Stöffler et al., 2018). At higher shock stages (C—S5 and C—S6, >35 GPa, Stöffler et al., 2018; Moreau et al., 2019a) the onset of iron sulfide, metal, and silicate melting can be observed at different degrees of intensity. At shock stages C—S5 and C—S6 the first phases to melt by shock are plagioclase and FeNi-FeS eutectic mixtures (>30–45 GPa, Stöffler et al., 1991, 2018, Moreau et al., 2019a), followed by iron sulfides (>40 GPa, Moreau et al., 2019a). Amorphization of plagioclase by shock can be caused either by the formation of diaplectic glass (Stöffler et al., 1991; Stöffler, 2000; Fritz et al., 2017; Stöffler et al., 2018) from solid-state amorphization (Jaret et al., 2015; Fritz et al., 2017) or by the formation of a quenched dense melt at high pressure (Chen and El Goresy, 2000) which, contrary to diaplectic glass, displays flow textures and voids (Yamaguchi and Sekine, 2000; Fritz et al., 2017). Since our modeling approach focuses on the process of shock melting and is not designed to simulate solid-state amorphization, we address only one of the possible formation mechanisms of plagioclase glass in this study. Iron sulfides melt at their grain borders (Bennett and McSween Jr., 1996), or as isolated droplets in silicate shock veins (Bennett and McSween Jr., 1996); Sharp et al., 2015), and display intermixed melting with plagioclase (Moreau, 2019), depending on the shock conditions (Moreau et al., 2018a, 2019a).

* Corresponding author at.: Ravila 14A, 50411, Tartu, Estonia.
E-mail addresses: juulia.moreau@ut.ee, juulia.moreau@helsinki.fi (J.-G. Moreau).

https://doi.org/10.1016/j.pepi.2020.106630
Received 6 May 2020; Received in revised form 26 October 2020; Accepted 7 December 2020
Available online 10 December 2020

Melting of iron sulfides is also observed associated with melting of metals in eutectic mixtures (Ohno, 1987; Chen et al., 2002; Tomkins, 2009; Lehner et al., 2010; Wang et al., 2011; Horstmann et al., 2013); in such cases, the melt composition is dominated by iron sulfides. Melting of metals as isolated grains is rarely observed (Bennett and McSween Jr., 1996). However, in shock veins of ordinary chondrites where pore collapse generates very high shock temperatures (Stöffler et al., 1991, 2018; Güldemeister et al., 2013; Sharp et al., 2015; Levesque and Vitello, 2015; Hu and Sharp, 2017; Moreau et al., 2018a, 2019a) or in highly porous materials (Bland et al., 2014), melting of metals is often observed as melt droplets or as intermixed melting with silicates (e.g. olivine, pyroxene or plagioclase, Tomkins, 2009). In general, melting of olivine and pyroxene is observed in shock veins or at pressures above 75 GPa (whole-rock melting, Stöffler et al., 1991, 2018). Shock melting occurs also from frictional heating between grains (van der Bogert et al., 2003) or from localized deformation in shear bands (Schmitt et al., 1987; Ebert et al., 2018).

Shock-darkening, as we refer to in this work, is a melting feature associated with iron sulfides and metals and happens at the transition between C—S5 and C—S6 (40–60 GPa, Moreau et al., 2019a and references therein), affecting large areas in ordinary chondrites. Shock melted iron sulfides and metals migrate into cracks between the solid silicate grains (Tomkins et al., 2013) and form a network of micron to submicron melt veins (Heymann, 1967; Britt et al., 1989; Britt and Pieters, 1989, 1994; Stöffler et al., 1991; Keil et al., 1992; Kohout et al., 2014). The network of veins optically darkens the lithology and alters the reflectance spectra (Kohout et al., 2014) with possible implications for asteroid reflectance spectra and their classification (DeMeo et al., 2009; DeMeo and Carry, 2014). Eutectic melting of mixtures between iron sulfides and metals is likely an important factor facilitating shock-darkening (Tomkins et al., 2013), considering that >80% of metal grains in ordinary chondrites are in contact with iron sulfides (Mare et al., 2014). Shock-darkening was observed in ordinary chondrites of shock stages C—S5 and C—S6 (Rubin, 1992; (Bennett and McSween Jr., 1996); Rubin et al., 1997; Wang et al., 2011; Kohout et al., 2014) but only in few individual samples, because LL and H-chondrites of shock stages C—S5 and C—S6 are generally rare (Bischoff et al., 2018). Also, in the estimated typical pressure range of 40–60 GPa for C—S5 and C—S6 ordinary chondrites (Moreau et al., 2019a), shock-darkening may not occur in all cases. For example, the ordinary chondrites Chelyabinsk LL5 (~50 GPa estimated pressure, Kohout et al., 2014, Kohout et al., 2020, Moreau et al., 2019a, Moreau, 2019) and McKinney L4 (C—S6, (Bennett and McSween Jr., 1996) were both naturally shock-darkened while shock-darkening was not observed in Kingfisher L5 (C—S6, (Bennett and McSween Jr., 1996) containing only isolated droplets of molten iron sulfides. In few cases, shock-darkening also happens locally in the vicinity of shock melt veins in meteorites that recorded lower shock stages (C—S2 to C—S4), in experiments inducing frictional heating (van der Bogert et al., 2003) or in shock compression experiments with porous ordinary chondrite (>30% initial porosity, Hirata et al., 2009). These observations indicate that the peak shock pressure alone is not a reliable predictor for the degree of shock-darkening and additional factors need to be considered. Important parameters influencing the degree of shock-darkening include the porosity of the meteorite before shock, which influences the intensity of shock heating (Moreau et al., 2019a), the heating and cooling history of the migrating molten iron sulfides and metals (Tomkins et al., 2013), and the effect of pre-shock temperatures (Schmitt, 2000) on the required pressures for shock-darkening (Moreau et al., 2019a). Shock-darkening was reproduced in high pressure shock-recovery experiments over a range of different pressures and pre-shock sample porosities (e.g. Schmitt, 2000, Moreau, 2019, Bezaeva et al., 2010, Kohout et al., 2020) but a systematic study of the influence of individual experimental parameters is still pending. Therefore, the conditions necessary for shock-darkening are not yet fully understood. Aside from shock-darkening induced by shock melt veins of metals and iron sulfides, as we address it in this work, darkening of the lithology can also occur as a result of whole rock shock melting (Stöffler et al., 2018; Kohout et al., 2020) or in localized silicate shock veins containing metal and iron sulfide droplets (Sharp et al., 2015).

To investigate the effects of shock compression, several studies implemented mesoscale (mm-scale) numerical models of heterogeneous media (e.g. Güldemeister et al., 2013, Bland et al., 2014, Davison et al., 2016, 2017, Moreau et al., 2017, 2018a, 2019a, Moreau, 2019). A few of these studies (Moreau et al., 2017, 2018a, 2019a) focused specifically on ordinary chondrites considering materials such as olivine, pyroxene, albite, troilite, and iron, as well as open pores to represent the major phases and texture of these meteorites. They used the iSALE-2D shock physics code (Amsden et al., 1980; Melosh et al., 1992; Ivanov et al., 1997; Collins et al., 2004, 2011; Wünnemann et al., 2006) in order to study post-shock heating and melting of the phases listed above, with special focus on the formation of shock-darkening. Using this approach, Moreau et al. (2018a, 2019a) found that 1) post-shock temperatures are heterogeneously distributed with strong temperature contrasts between individual grains of different phases (e.g. >400 K between metals and iron sulfides, or silicates) and 2) at pressures between 30 and 70 GPa iron metal is not heated as efficiently as iron sulfides by shock entropy, so that immediate melting of iron metal by shock is limited.

To investigate the effects of shock compression, several studies implemented mesoscale (mm-scale) numerical models of heterogeneous media (e.g. Güldemeister et al., 2013, Bland et al., 2014, Davison et al., 2016, 2017, Moreau et al., 2017, 2018a, 2019a, Moreau, 2019). A few of these studies (Moreau et al., 2017, 2018a, 2019a) focused specifically on ordinary chondrites considering materials such as olivine, pyroxene, albite, troilite, and iron, as well as open pores to represent the major phases and texture of these meteorites. They used the iSALE-2D shock physics code (Amsden et al., 1980; Melosh et al., 1992; Ivanov et al., 1997; Collins et al., 2004, 2011; Wünnemann et al., 2006) in order to study post-shock heating and melting of the phases listed above, with special focus on the formation of shock-darkening. Using this approach, Moreau et al. (2018a, 2019a) found that 1) post-shock temperatures are heterogeneously distributed with strong temperature contrasts between individual grains of different phases (e.g. >400 K between metals and iron sulfides, or silicates) and 2) at pressures between 30 and 70 GPa iron metal is not heated as efficiently as iron sulfides by shock entropy, so that immediate melting of iron metal by shock is limited.

The degree of post-shock heating and melting as a function of shock stage predicted by the models of Moreau et al. (2018a, 2019a) is in good agreement with the shock classification of ordinary chondrites (Stöffler et al., 1991, 2018). However, their models fail to reproduce the high degrees of melting of metals in eutectic mixtures, intermixed melting of metals and silicates (Moreau et al., 2019a, Fig. 6, annot. 2; Tomkins, 2009, Fig. 2A and 3B; Tomkins et al., 2013, Fig. 2), and melting of phases in the vicinity of hotspots from closure of cracks, hence underestimating shock melting in ordinary chondrites, including the high pre-shock temperatures conditions (up to ~920 K) of internal heating processes on their parent asteroids (Schmitt, 2000; Moreau et al., 2019a). Also, these models can not explain the presence of metals in the shock-darkening veins that is observed in ordinary chondrites (Stöffler et al., 1991).

One major shortcoming of the numerical models of Moreau et al. (2018a, 2019a) that could explain the discrepancies between models and observations, lies in the perpetuation of strong temperature contrasts among different phases. Such temperature contrasts are preserved in iSALE models, since heat diffusion during or after shock is not considered in the code. Upon shock heating, strongly heated phases would transfer heat to the surrounding cooler phases (Tomkins, 2009; Shaw and Walton, 2013; Sharp et al., 2015; Hu and Sharp, 2017) and metals that did not melt during shock could be molten subsequently by the heat from adjacent grains. This process could potentially explain the observed eutectic melting of metals in shocked ordinary chondrites and their presence in the shock-darkening veins.

Recent studies (Sharp et al., 2015; Hu and Sharp, 2017) focused on

Table 1
Model parameters.

Model[a]	Texture[b]	Grid dimensions (*nx*, *ny*)[c]	Boundary temperatures (K) (top, bottom, left, right)[d]	Model Variations[e]
1 (1)	iron grain	400 × 238	1005, 1003, 940, 940	a) 6% pre-shock porosity in olivine
			1571, 1522, 1479, 1479	b) 15% pre-shock porosity in olivine (adjusted to 50.0 GPa[f])[g]
				→ b) additional: cell size = 2 μm
				→ b) additional: olivine thermal diffusivity × 3
2 (2)	troilite grain	400 × 238	941, 1034, 921, 921	a) 6% pre-shock porosity in olivine
			1471, 1513, 1446, 1446	b) 15% pre-shock porosity in olivine (adjusted to 50.0 GPa[f])
3 (6)	troilite grain in iron grain (eutectic)	400 × 238	1053, 1096, 950, 950	
4 (8)	troilite grain atop iron grain (eutectic)	400 × 200	902, 932, 860, 860	a) at 46.7 GPa
			984, 998, 924, 924	b) at 49.9 GPa
			1057, 1070, 991, 991	c) at 53.1 GPa
			1135, 1146, 1062, 1062	d) at 56.3 GPa
			1228, 1224, 1135, 1135	e) at 59.7 GPa
5 (17)	mosaic of iron grains in troilite (eutectic)	800 × 476	951, 1089, 924, 924	a) small iron inclusions (30 cells)
			958, 1083, 926, 926	b) medium troilite inclusions (50 cells)
			951, 1089, 924, 924	c) large iron inclusions (58 cells)
6 (18)	mosaic of troilite grains in iron (eutectic)	800 × 476	1019, 1037, 935, 935	a) small troilite inclusions (30 cells)
			1025, 1058, 933, 933	b) medium troilite inclusions (50 cells)[h]
			1008, 1067, 928, 928	→ b) additional: H-chondrite
				→ b) additional: L-chondrite
				→ b) additional: LL-chondrite
				c) large troilite inclusions (58 cells)
7 (22)	albite grain	400 × 268	918, 994, 922, 922	a) nonporous albite
			918, 1022, 921, 921	b) 6% porous albite
8	albite insert in iron grain (bottom)	400 × 238	997, 1008, 938, 938	nonporous albite
9	albite insert in iron grain (top)	400 × 238	971, 1013, 935, 935	a) nonporous albite
			986, 1013, 937, 937	b) 6% porous albite
10	model 4 with troilite inclusions in iron (eutectic)	400 × 200	977, 1014, 923, 923	
11	troilite grain with albite insert on top	400 × 238	801, 950, 797, 797	a) 6% porous albite, 43.7 GPa
			865, 1016, 858, 858	b) 6% porous albite, 46.7 GPa
			931, 1084, 922, 922	c) 6% porous albite, 49.9 GPa
12	troilite grain with peripheral albite on top	400 × 238	806, 923, 797, 797	a) 6% porous albite, 43.7 GPa
			868, 987, 857, 857	b) 6% porous albite, 46.7 GPa
			935, 1054, 921, 921	c) 6% porous albite, 49.9 GPa
N1 (N1)	enstatite chondrite heterogeneous model	900 × 919[i]	1832 1793 1820 1820	

(a) Models 1–7 and N1 (or some of their variations) reproduce model setups published by (Moreau et al., 2018b; Moreau et al., 2019a). The numbers in brackets are the corresponding model labels from those publications.
(b) grain configurations in the olivine matrix.
(c) $dy = dx = 1$ μm.
(d) all left and right boundaries are identical since the models are axial-symmetric along a vertical axis of symmetry. Any boundary is only composed of olivine.
(e) All described grain configurations are embedded in an olivine matrix. Unless stated otherwise, the pre-shock porosity of olivine is 6% and the pre-shock porosities of all other phases are 0%.The pressure load is 49.9 GPa if not stated otherwise.
(f) this pressure value is only slightly higher than other models at 49.9 GPa in regard to the model set-up (velocity of the flyer plate, (Moreau et al., 2018a)
(g) two extra models are used, with: twice the cell size or thrice the olivine diffusivity.
(h) Model 6b is also declined in 3 other models where values of eutectic melting temperatures and heats of fusion are adapted from Mare et al. (2014) to represent H, L and LL chondrites.
(i) $dy = dx = 1.34$ μm.

heat diffusion in 1-D and 2-D in shocked melt veins of silicates in chondrites, assuming initial shock temperatures from Hugoniot data. In this work we will extend this approach of post-shock diffusion modeling by considering iron metal, iron sulfides (troilite) and plagioclase (albite) in an olivine matrix with initial temperature distributions derived from 2-D post-shock temperature maps of iSALE models similar to those used in Moreau et al. (2018a). Using this approach we investigate the effect of diffusive heating on the melting of different phases in shock heated chondrites and evaluate the significance of diffusive heating for the formation of shock features that could not be reproduced in earlier models.

2. Methods

2.1. Model setup

In order to investigate the role of diffusive heating in different grain configurations that occur in ordinary chondrite textures (e.g. Tomkins, 2009; Moreau et al., 2018a, 2019a; Moreau, 2019), we set up 12 base models with different arrangements of iron, troilite and albite grains in an olivine matrix (Table 1). The models are designed to investigate the melting of single grains of iron (model 1), troilite (model 2), and albite (model 7) in a homogeneous olivine matrix, as well as eutectic mixtures of iron and troilite with different textural configurations (models 3, 4, 5, 6 and 10) and intermixed melting of metals or iron sulfides with silicates (models 8, 9, 11 and 12). The grain configurations of the 12 base models are displayed in Figs. 1 and 2. In order to explore also the effects of other parameters than the grain configuration we set up several variations of these models, varying shock pressures (models 4a-e, 11a-c and 12a-c), grain sizes (models 5a-c and 6a-c), grain shapes (models 11a-c and 12a-c), and pre-shock silicate porosities (models 1a-b, 2a-b, 7a-b and 9a-b).

If not stated otherwise, all models were shocked at a nominal pressure of 50 GPa (Moreau et al., 2017), which corresponds to the middle of

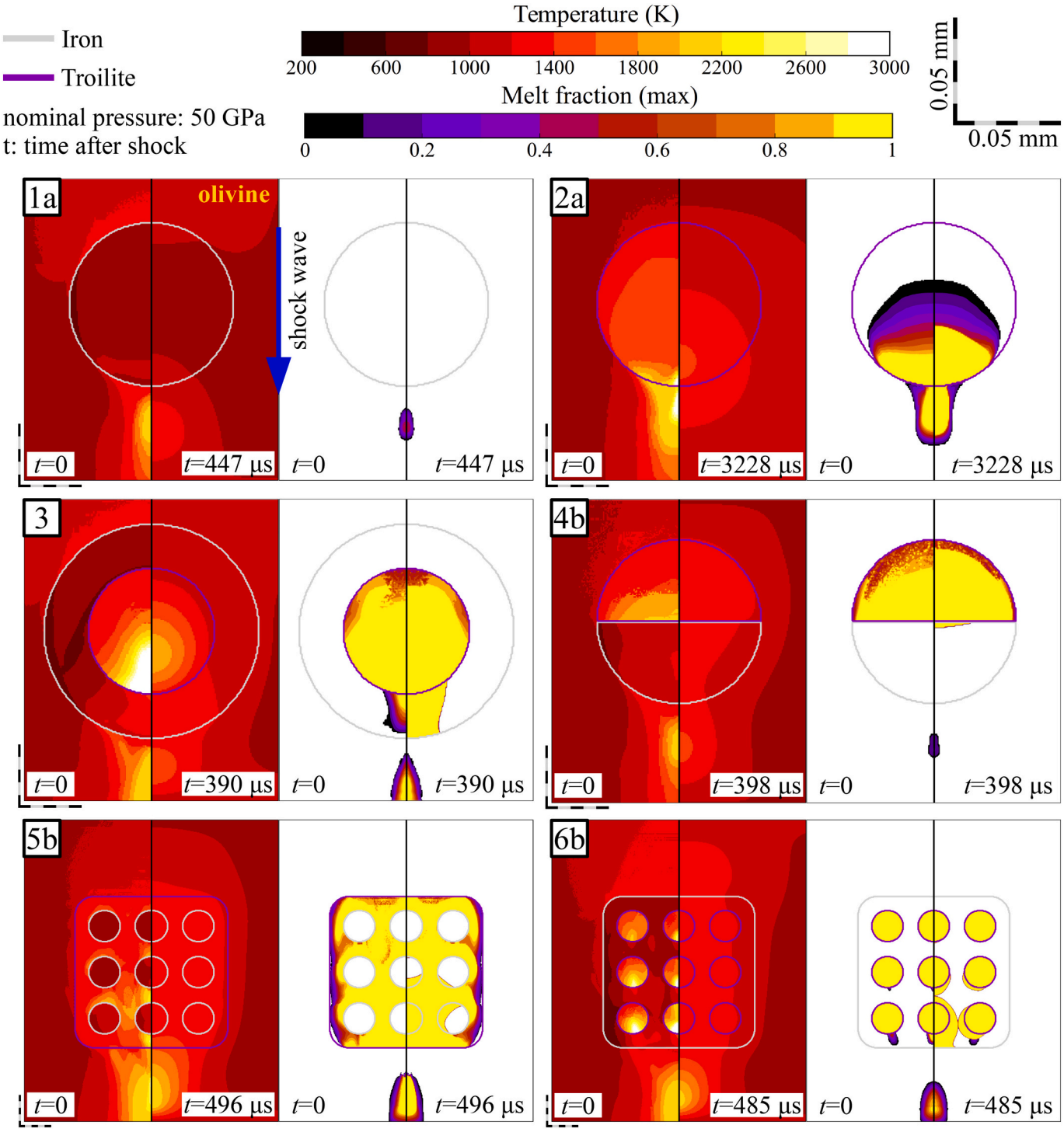

Fig. 1. Heating and melting in models 1–6. For each model the left panels display 2-D temperature maps and the right panels display 2-D melt fraction maps. Each panel is subdivided to represent the initial condition after shock (input for the diffusion model, state at time *t*: 0 µs) and the properties after a specific diffusion time (output of the diffusion model). Note: the displayed melt fractions are the maximum melt fractions recorded at a given grid point up until the specified diffusion time – regardless if the phase has solidified at the marked time. The areas that did not experience any melting are shown in white. Color outlines in the 2-D maps are material boundaries with olivine as the matrix material. Nominal pressure (pressure recorded in the iSALE model buffer plate, Moreau et al., 2017) is 50 GPa. All models, except model 3, have several variations (e.g. change in nominal pressure, porosity, grain size), but this figure only shows one of those variations labeled with letters. All model parameters are summarized in Table 1. (For interpretation of the references to color in this figure legend, the reader is referred to the web version of this article.)

the pressure range of 40–60 GPa proposed for shock-darkening (Moreau et al., 2019a). The pre-shock porosity in the models was typically assumed to be 6% for the olivine matrix and 0% for iron, troilite and albite grains. In order to study the effect of higher pre-shock porosities on the local post-shock temperatures, we raised the olivine porosity to 15% and the albite porosity to 6% in some models. Those porosities lie in the range of porosities observed in ordinary chondrites (Consolmagno et al., 1998; Britt and Consolmagno, 2003; Sasso et al., 2009;

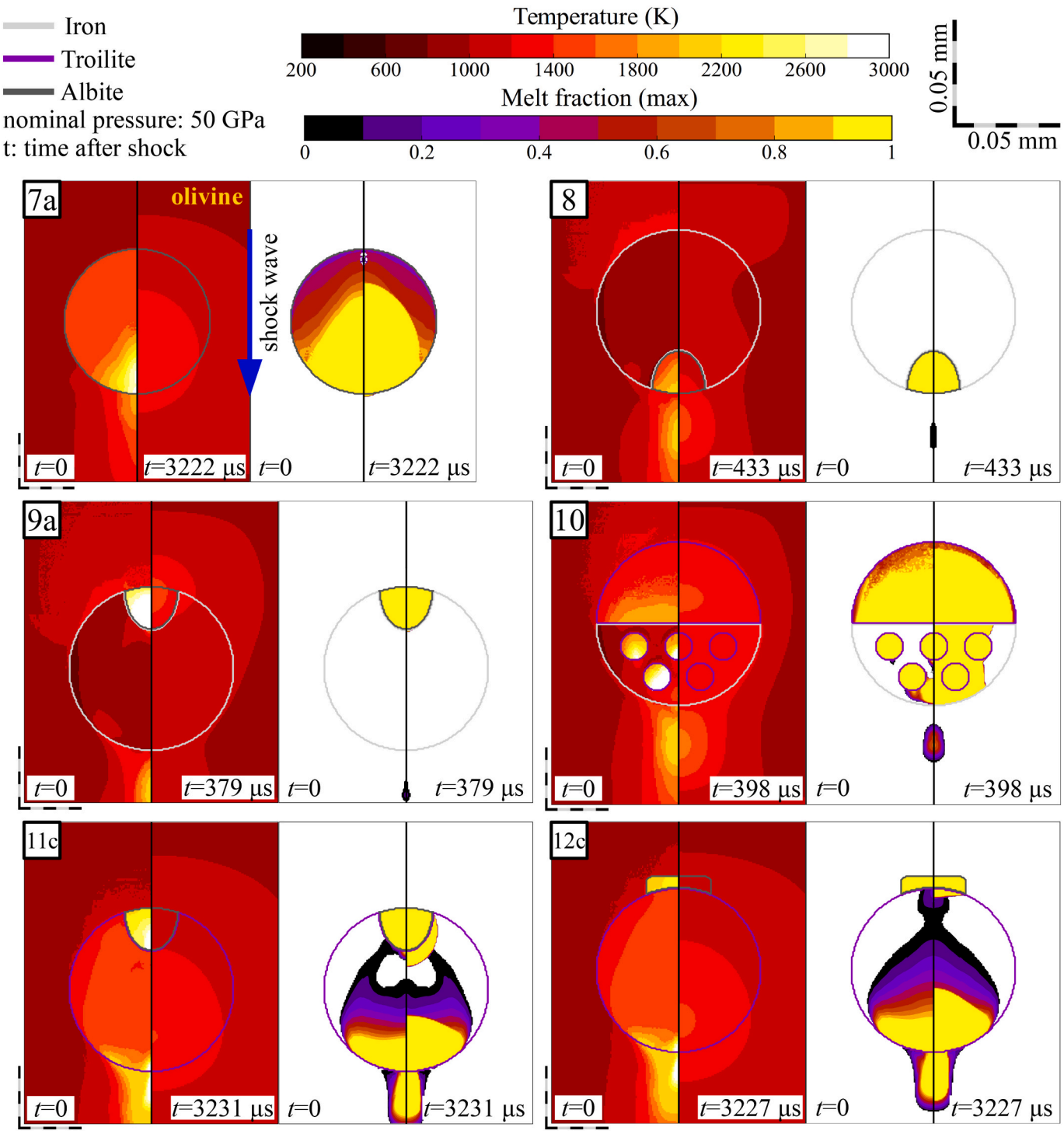

Fig. 2. Heating and melting in models 7–12. For each model the left panels display 2-D temperature maps and the right panels display 2-D melt fraction maps. Each panel is subdivided to represent the initial condition after shock (input for the diffusion model, state at time *t*: 0 µs) and the properties after a specific diffusion time (output of the diffusion model). Note: the displayed melt fractions are the maximum melt fractions recorded at a given grid point up until the specified diffusion time – regardless if the phase has solidified at the marked time. The areas that did not experience any melting are shown in white. Color outlines in the 2-D maps are material boundaries with olivine as the matrix material. Nominal pressure (pressure recorded in the iSALE model buffer plate, (Moreau et al., 2017) is 50 GPa. All models, except models 8 and 10, have several variations (e.g. change in nominal pressure, porosity, grain size), but this figure only shows one of those variations labeled with letters. All model parameters are summarized in Table 1. (For interpretation of the references to color in this figure legend, the reader is referred to the web version of this article.)

Consolmagno et al., 2008) and reflect the complex processing of the material by multiple shock events and thermal metamorphism since the formation of their parent bodies. Assuming this range of porosities also allows us to compare our results to shock-recovery experiments on naturally shocked ordinary chondrites (9% porosity, Schmitt, 2000; 12%, Bezaeva et al., 2010; 6%, Kohout et al., 2020) and verify the applicability of our approach. Porosities of primitive ordinary chondrites can reach values of >30% (Hirata et al., 2009; Bland et al., 2014).

However, to limit the number of models in this study and being aware of limitations of our models regarding the treatment of pore collapse, we restrict the range of assumed porosities to lower values, which are more representative for thermally metamorphosed ordinary chondrites (0–20% porosity, Consolmagno et al., 2008) and to the conditions met in shock experiments (Langenhorst and Deutsch, 1994; Langenhorst and Hornemann, 2005).

2.2. Shock deformation, heating and melting

The textural models described above serve as input for the iSALE model that simulates deformation, heating and melting of the material, which we later use as input for our diffusion model. The setup of the iSALE model is designed to simulate planar shock experiments (e.g. Kowitz et al., 2013), where the sample is shocked by a plate impacting from above, so that the shock wave travels through the sample along its vertical axis. For an in-depth discussion of the model setup used in this study and the calculation of post-shock temperature (assuming adiabatic release after shock) and melting (considering heat of fusion) in the iSALE code we refer to the work of Moreau et al. (2017, 2018a, 2019a, 2019b), whose approach we adapted for our study. The method for adiabatic release used in the aforementioned works and this study provides a first order estimate of post-shock temperatures through phase changes in olivine or iron, although the exothermic effect of back-transformation of phases from shock release (e.g. iron, Hwang et al., 2020) and the back-transformation of phases from cooling (Hu and Sharp, 2017) are neglected. Indeed, the release of the shock will not be perfectly isentropic with the formation of metastable minerals (phase transitions), but it has been argued in previous studies that this discrepancy is negligible with respect to the entropy of the shock, so that an isentropic release remains a good approximation of shock release affected by phase transitions (e.g. quartz; Luo et al., 2003, Kraus et al., 2012).

To study the degree and local distribution of shock heating, we produce post-shock temperature and melt fraction maps for each of our textural models. Initial material properties are discretized in a Cartesian mesh of equal *dx* and *dy*, in which changes of temperature and melt fraction are recorded during the shock event. The positions of material nodes are displaced by shock compression, as the material is deformed, resulting in an unevenly spaced mesh that cannot be readily transferred to a diffusion code with equidistant nodes. However, material deformation is limited in the models assumed in this study and has no significant effect on the temperatures and melt fractions of phases. Hence we decided to use the original Cartesian node positions of the cells when transferring post-shock temperatures and material properties to our diffusion code. However, it should be noted that settings involving strong deformation, e.g. during pore crushing (Moreau et al., 2018a), could not be modeled using this approach but would require an explicit transfer of local material properties from the deformed iSALE mesh to the diffusion code to obtain reliable results. In the *Supplementary Material* (section 1) we present a pore crushing model from Moreau et al. (2018a) compared to model 5b to illustrate the degrees of deformation mentioned above. Since our current modeling approach is not suited for the explicit modeling of macroporosity (voids) and the resulting material deformation, we assume that the porosity occurs as microporosity and hence treat porosity solely as a material parameter as in Wünnemann et al. (2006). However, further development of the code by implementation of the required features for modeling pore crushing might be useful for future studies of the effects of macroporosity, including the effects of pore shape and the orientation of the pore to the shock wave on shock heating (see details in Levesque and Vitello, 2015, Moreau et al., 2017, 2019a).

We assume that the shock wave compresses the material to 0% porosity, dismissing the formation of porosity during material relaxation (e.g. by the opening of cracks), after the shock wave has subsided. Consequently, porosity as considered in this study has only an effect on post-shock heating but does not affect later heat diffusion.

Because 2-D models with the iSALE or diffusion code ran from a few hours to a week, we saved computation time by avoiding the use of time consuming 3-D models (up to a few months of calculations in either the iSALE or the diffusion code). To allow for a 3-D behavior of the shock wave within spherical grains in the 2-D geometry of iSALE, we placed the circular grains along an axis that allows cylindrical symmetry calculations in models. The axis is parallel to the direction of the shock wave. Circular 2-D grains that are placed on the central symmetry axis translate to spherical grains in the 3-D cylindrical geometry, so that using a cylindrical geometry allows us to simulate the 3-D behavior of the shock wave in spherical grains in our 2-D models. However, in the cylindrical geometry spherical grains can only be simulated accurately if they are placed on the cylindrical symmetry axis, because circular 2-D grains that are placed further away from the central axis do not translate to spherical grains but to tori placed around the rotational axis. Hence, in grains positioned away from the cylindrical symmetry axis, the propagation of shock waves differs from that in spherical grains, which can lead to changes in shock wave attenuation or convergence depending on the grain geometry and its location away from the axis of symmetry (see *Supplementary Material, section 4*; Moreau et al., 2018a). Similarly, the 2-D diffusion code tends to underestimate the dissipation of heat by neglecting the 3rd dimension.

Assessing the minimal amount of constitutive cells in rounded grains (resolution) is important to offer the best quantitative and qualitative estimates on heating and melting with a minimal error (Moreau et al., 2017, 2018a, 2019a). We replicated such a resolution study (see results in *Supplementary Material*, section 5) and found out that the error is minimal (melt fraction, <1%) for smallest grains of 15 cells radii such as in models 5–6.

2.3. Post-shock heat diffusion

We simulate the relaxation of temperature contrasts in the post-shock temperature maps produced by iSALE using a 2-D finite difference code for multi-phase meshes (olivine, iron, troilite, albite, pyroxene) based on the heat diffusion equation

$$\frac{\partial T}{\partial t} = D\left(\frac{\partial^2 T}{\partial dx^2} + \frac{\partial^2 T}{\partial dy^2}\right) \tag{1}$$

which we solve applying an explicit finite difference scheme, assuming $dx = dy$ and considering discontinuities in local diffusivity values (Praprotnik et al., 2004):

$$T_{i,j}^{k+1} = T_{i,j}^{k} + dt\frac{\left(D_{i-1/2,j}\left(T_{i-1,j}^{k} - T_{i,j}^{k}\right) + D_{i+1/2,j}\left(T_{i+1,j}^{k} - T_{i,j}^{k}\right) + D_{ij-1/2}\left(T_{ij-1}^{k} - T_{i,j}^{k}\right) + D_{ij+1/2}\left(T_{ij+1}^{k} - T_{i,j}^{k}\right)\right)}{dx^2} \tag{2}$$

where dt is time step, T is temperature, dx and dy are distances between nodes along the x- and y-axis of the mesh, respectively, D is thermal diffusivity, i and j are node indexes, and k is the iteration number.

We assumed constant Dirichlet boundary temperatures corresponding to the average temperatures of the cells along the edges of the iSALE

models. The particles embedded in the olivine matrix at the center of the model are at a distance of at least 30 to 100 cells from the model edges. Hence the boundary temperatures do not affect the temperatures in the area of interest around individual shock heated grains or hotspots in the surrounding olivine matrix in the time scales considered in the diffusion models. In the *Supplementary Material*, we provide a test on model 2a with larger distances between the central area of interest and the model edges to illustrate to which degree the distance to the model edges affects our results.

2.3.1. Melt fraction and latent heat

The redistribution of heat by diffusion leads not only to changes in temperature but also in the physical state of the material, i.e. partial or complete melting of initially cooler phases and (partial) crystallization of phases that were initially molten by shock. Therefore we need to consider the latent heat of melting (or fusion) and track the local material state in order to determine more accurate local temperatures. Since we do not model the diffusion of heat but the diffusion of temperature, we consider latent heat in the diffusion code by introducing the virtual temperature change ΔT_{latent} that would result from adding the respective amount of heat to the system without a phase change, assuming the heat capacity at the melting temperature (Hu and Argyropoulos, 1996):

$$\Delta T_{latent} = H_f / c_{p-melt} \tag{3}$$

where H_f is the heat of fusion and $c_{p\text{-}melt}$ is the heat capacity at the melting temperature. Any temperature rise in solid material predicted by the diffusion code within ΔT_{latent} above the melting temperature (or within ΔT_{latent} below the melting temperature for a temperature decrease in molten material, respectively) is buffered by the code, simulating thermal buffering by latent heat (see e.g. Mare et al., 2014). The respective values for the ΔT_{latent} of each model phase are listed in Table 2. Note that in our model we treat all phases as pure phases in the sense that we assume single melting temperatures and do not explicitly consider solidus and liquidus temperatures of solid solutions. However, the error introduced by this simplification is small enough to allow a general assessment of melt fractions, considering, for example, the variability of individual mineral compositions in different types of ordinary chondrites (see *Supplementary Material* for a more detailed discussion). The assumed melting temperatures are 2049 K, 1429 K, 1811 K, and 1463 K for olivine (Fo_{90}), albite (An_{10}), iron, and troilite, respectively, following the approach of Moreau et al. (2018a). For eutectic mixtures of iron and troilite we assume a melting temperature of 1261 K, similar to models used in Moreau et al. (2018a, 2019a).

Within the diffusion code we calculate the melt fraction in partially molten material assuming a linear correlation between the melt fraction and the amount of heat added after reaching the melting temperature. For this purpose we introduce another virtual or fictive temperature ($\Delta T'$) which records the progression of partial melting over the temperature interval ΔT_{latent} with:

$$F = \Delta T' / \Delta T_{latent} \tag{4}$$

Table 2
Thermal parameters for the numerical materials.

Material	H_f(kJ/kg)[(a)]	$c_{p\text{-}melt}$(J/kgK)[(a)]	T_{melt}(K)[(a)]	ΔT_{latent}(K)
olivine	909	1469	2049	619
pyroxene[(b)]	650	1392	1832	467
albite	243	1253	1429	194
iron	292	806	1811	362
iron (eut.)	285	616	1261	439
troilite	368	852	1463	432
troilite (eut.)	285	744	1261	364

(a) values used in Moreau et al. (2018a, 2019a), see also references therein. Values are rounded from those used in the code.
(b) used only in the enstatite chondrite model N1.

where $\Delta T'$ equals zero, at the start of partial melting, and equals ΔT_{latent}, at complete melting.

2.3.2. Thermal diffusivities

After each time step, we update the local thermal diffusivities corresponding to the current local temperatures and types of material and adjust the length of the subsequent time step accordingly, considering the stability criteria for the finite difference scheme used in our diffusion code:

$$dt = \frac{dx^2}{16 D_{max}} \tag{5}$$

We considered thermal diffusivities of different materials as a function of temperature based on experimental data by Monaghan and Quested (2001), Gibert et al. (2005), Hofmeister (2012) and Branlund and Hofmeister (2012) for iron, olivine, pyroxene, and albite, respectively. The thermal diffusivity of troilite was estimated using a variation of heat conductivity with temperature similar to iron (Table IV in Abu-Eishah, 2001), with an initial heat conductivity of troilite from Yomogida and Matsui (1983) and applying the change of heat capacity over temperature for troilite given in (Chase Jr., 1998). With these considerations, we obtain three equations for the thermal diffusivity of troilite (in m^2/s) at different temperature intervals of the form:

$$D = AT^3 + BT^2 + CT + E \tag{6}$$

The respective values for the coefficients A, B, C and E at each temperature interval are given in Table 3. The thermal diffusivities of liquid phases were not explicitly considered but assumed to be constant and equal to the thermal diffusivity of the solid phase at the melting temperature. We also assume that diffusion occurs after the shock wave has subsided, so that pressures are constant. Therefore, for all models we assume thermal diffusivities with an ambient pressure of ~0 GPa.

3. Results

Our work considers the combined effects of two processes controlling heating and melting during shock metamorphism in ordinary chondrites: increase of internal heat by the shock wave and redistribution of this heat by diffusion. These processes affect all phases to some degree, depending on the response of the phases to shock compression, impedance contrasts, texture and geometry of individual grains (e.g. Moreau et al., 2018a), which leads to significant contrasts in local post-shock temperatures.

Heat diffusion leads to the relaxation of temperature contrasts between strongly heated and moderately heated areas of the sample. Thereby initially cooler areas can be heated by neighboring hot spots and experience periods of partial or complete melting before the sample eventually cools to subsolidus temperatures. Since we were interested in the maximum degree of melting that can be reached in the sample, we stopped the diffusion algorithm typically after every area of the sample had begun cooling from its maximum temperature, ensuring that no more melt could be produced. The melt fractions shown in Figs. 1 and 2 are the maximum melt fractions recorded for each individual cell during the runtime of the model. The diffusion times at which the models were terminated vary depending on the time scale at which individual model textures could equalize local temperatures. Hence, the selected diffusion times are shorter for models containing highly thermally conductive phases like iron metal or having smaller grain sizes, than for models containing mostly phases with low thermal conductivity or larger grain sizes. All results for shock heating and diffusion of heat after time t are compiled in Figs. 1 and 2 and in Table A.1 (*Supplementary Material*) that compiles peak shock pressures, initial and final post-shock temperatures and melt fractions recorded from the iSALE and diffusion models (see Table 1 and section 2). Temperatures, melt fractions, or thermal diffusivities compiled in Table A.1 and all figures in this work are an average

Table 3
Coefficients for troilite thermal diffusivity over temperature used in the models.

Temperature interval (K)	*A*	*B*	*C*	*E*
293–411	$6.5339624 \times 10^{-13}$	$-6.9034131 \times 10^{-10}$	$2.32666298 \times 10^{-7}$	$- 2.360408239 \times 10^{-5}$
411–598	0	$1.549034062 \times 10^{-12}$	$-2.4932287099 \times 10^{-9}$	$1.7673091035 \times 10^{-6}$
598–1463	0	$-1.82121918322 \times 10^{-13}$	$-1.591504802 \times 10^{-10}$	$1.1298507534 \times 10^{-6}$

Troilite thermal diffusivities are calculated with the listed coefficients using eq. (6).

of all cells assigned to a specific phase. In the following we summarize the results, focusing on the observed degrees of heating, melting and cooling in our models and the specific effects of different parameters on the melt fractions produced in the sample.

3.1. Phase specific contributions of shock heating and diffusion to melting

The contributions of initial shock heating and subsequent post-shock diffusion on the degree of melting vary among different phases. Melting of troilite (models 2–6 and 11–12), olivine (matrix in all models), and albite (models 7–12) is predominantly shock induced and reaches high melt fractions, i.e. 0.166 (model 2b) to 1.000 (model 6a) for troilite, and 0.765 for albite (model 7a). Heat diffusion affects melting of these phases only to a small degree, either as a result of local temperature heterogeneities within individual grains (observed in all models) or at contacts to other strongly shock-heated phases (olivine or troilite in contact with albite as in models 7a–b, 9b and 11–12). At contacts to cooler, weakly shock-heated phases the strongly shock-heated phases can experience extremely fast cooling (in the order of ~0.1–1 K/μs for the grain sizes considered here, e.g. cooling by 537 K in 485 μs in a troilite grain, model 6b) and associated fast solidification of any melt produced by the initial shock.

Shock melting of iron metal (models 1, 3–6 and 8–10) is rare, even in eutectic mixtures with troilite (0.097 melt fraction, model 10), because shock heating is less efficient in iron due to its impedance properties (Ahrens et al., 1998; Moreau et al., 2018a, 2019a). Significant heating and melting of iron metal occurs predominantly by diffusion of heat from strongly shock-heated neighboring phases, for example troilite (see Figs. 1, 2 and 12). As a consequence, melting of iron metal occurs much more rarely than melting of iron sulfides, which is consistent with observations in naturally shocked ordinary chondrites (Stöffler et al., 1991; Tomkins, 2009).

3.2. Effects of shock pressure

The shock pressure dictates the total amount of energy that can be transferred to the sample by the shock wave and is hence directly related to the observed degree of shock heating and melting. Increasing shock pressures do not only lead to higher overall post-shock temperatures, but also result in higher temperature contrasts between phases (see also Moreau et al., 2017, 2019a). This is because the fraction of energy converted into heat during passing of the shock wave remains similar for a given phase, according to their specific shock impedance properties. However, as the absolute shock wave energies increase with shock pressure, the absolute differences in post-shock temperatures among different phases increase as well. This effect can be observed in models 4a-e, 11a-c and 12 a-c where we imposed gradually increasing nominal pressures (47–60 GPa and 43–50 GPa, respectively). As expected, we observe increasing contrasts of post-shock temperatures between iron and troilite and stronger eutectic melting by diffusive heating in iron in models 4a-e (see Figs. 3a and 4a, Table A.1) and stronger temperature contrasts between albite and troilite and stronger melting by diffusive heating in models 11a-c and 12 a-c (see Fig. 5).

3.3. Effects of textural features

The texture of the sample, including the orientation, shape and size of individual grains as well as the sample porosity, has an effect on both the initial distribution of heat immediately after the shock and on the efficiency of subsequent redistribution of heat by diffusion.

3.3.1. Shock heating

Strong heating and melting is mostly observed 1) at the bottom of rounded grains where pressures converge and concentrate from the shock wave propagating from top to bottom, 2) in textures where low density phases are placed above high density phases and thus are heated by pressure reflections or 3) in textures containing porous phases, which facilitate local shock pressure concentrations by pore crushing.

Local heating in the olivine matrix below round grains due to local shock pressure concentrations is apparent in all models presented here (see Fig. 1). The degree of the local pressure concentration and associated heating depends on the impedance properties of the respective grain (i.e. iron, troilite and albite in models 1a, 2a and 7a, respectively) and the related extent of reflection and absorption of shock wave energy. Among the three phases iron (model 1a) has the highest impedance contrast to the surrounding olivine matrix, so that a significant amount of shock wave energy is reflected at the grain boundary, leading to heating of the matrix above the grain. The less dense troilite (model 2a) reflects less shock wave energy than iron, and albite (model 7a) shows virtually no heating of the overlying olivine matrix by shock wave reflection. The efficiency of shock wave absorption follows an inverse trend with iron absorbing only very little shock wave energy while troilite is much more strongly shock heated and albite shows the highest degree of shock wave absorption.

The effect of pressure reflections (Moreau et al., 2018a) can be observed comparing models 8 and 9a, where an albite grain is placed either at the top (model 9a) or at the bottom (model 8) of an iron grain. Initial post-shock heating of the albite grain is significantly more pronounced in model 9a, because the albite grain is passed both by the shock wave coming directly from the top of the sample and a reflection of this shock wave from the underlying iron grain. The albite grain in model 8 on the other hand is only passed by the initial shock wave passing through iron, which reduces the amount of energy transferred to the albite grain compared to the setting in model 9a. The differences in degree of shock heating and melting due to the different textures in models 8 and 9a are illustrated in Fig. 6.

The amount and distribution of porosity in a sample is a major factor influencing localized shock heating, since the compaction of pore space (pore crushing) is an efficient mechanism to absorb shock wave energy. In our models we varied the pre-shock porosity of the olivine matrix (6–15%, in models 1a-b and 2a-b) and of albite grains (0–6%, in models 7a-b and 9a-b). As expected, the higher the porosity of the material is, the higher are post-shock temperatures. The effect of porosity on the degree of heating and melting in an albite grain (model 9a-b) is illustrated in Fig. 6. Increased post-shock temperatures in the porous albite also lead to higher temperature contrasts to the surrounding matrix and, consequently, faster cooling rates of the albite grain (~0.3 K/μs in model 7b, compared to 0.1 K/μs in model 7a). Similarly, the initial porosity and resulting post-shock temperature of the matrix affects the thermal evolution of embedded grains by influencing the initial temperature

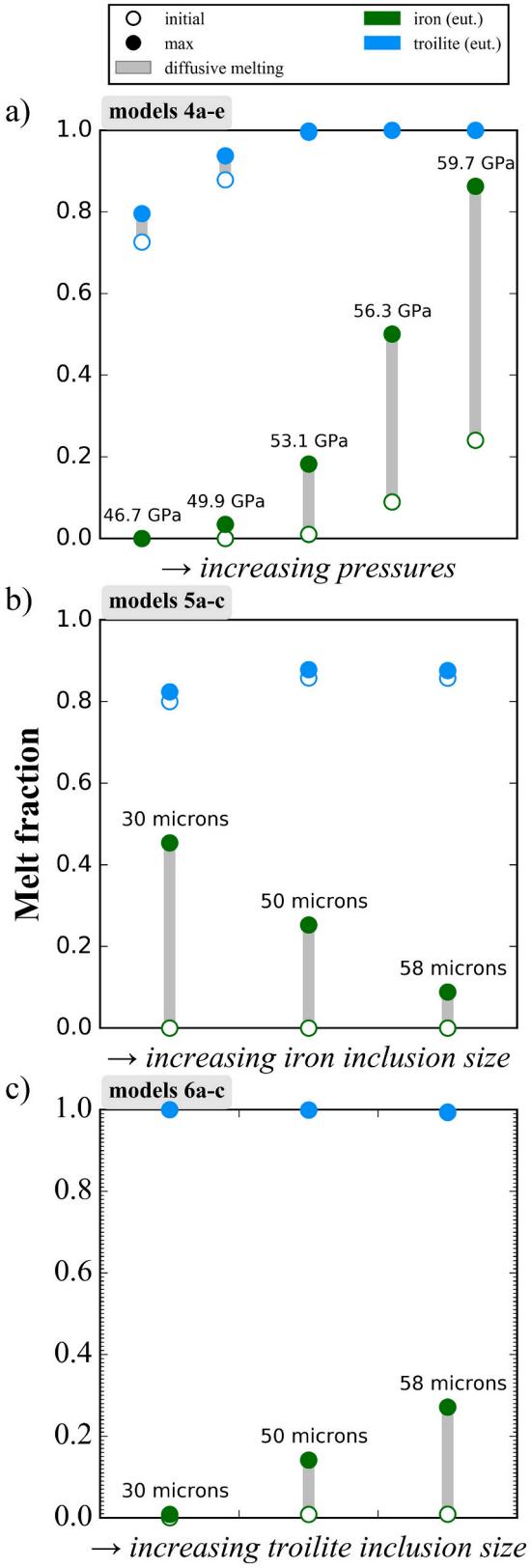

Fig. 3. Melt fractions in iron (green) and troilite (blue) grains before (open circles) and after (plain circles) heat diffusion, emphasizing on the effects of a) increasing pressures (models 4a-e), b) the size of iron inclusions in troilite (models 5a-c), and c) the size of troilite inclusions in iron (models 6a-c). Results corresponding to the same model are aligned at the same position along the horizontal axis. The values for the corresponding parameters in each model are indicated by black labels. The continuous gray bars between data correspond to the contribution of heat diffusion to the total melt fraction observed in the respective phase. (For interpretation of the references to color in this figure legend, the reader is referred to the web version of this article.)

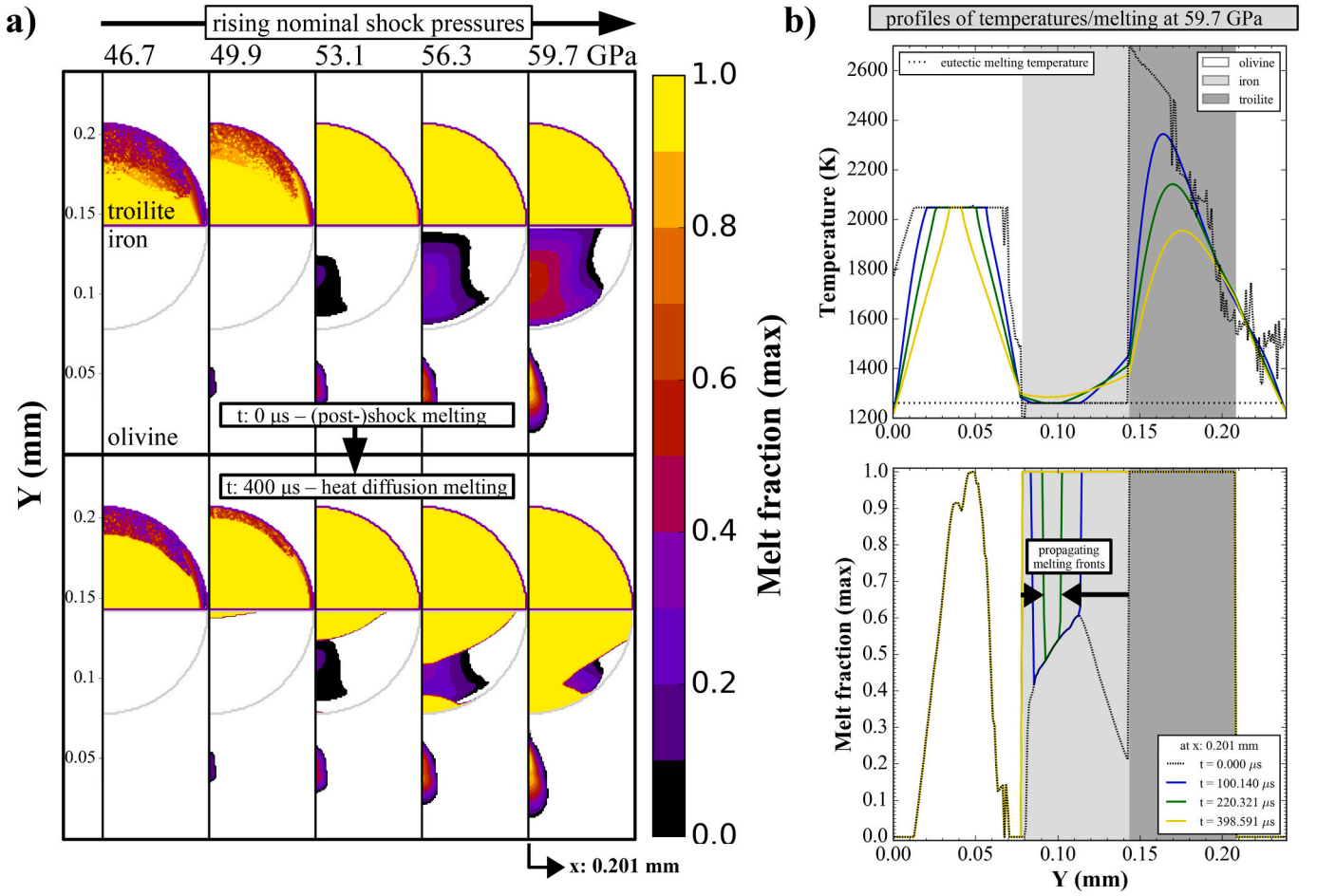

Fig. 4. Eutectic melting of iron and troilite in model 4, showing the effect of increased nominal pressure on the heat diffusion after shock. a) Individual melt fraction 2-D maps at initial and final conditions (~400 µs after the onset of heat diffusion) for each shock pressure. b) Evolution of temperatures and melt fractions along a cross section at x: 0.201 mm for model 4e (59.7 GPa). The areas that did not experience any melting are shown in white. (For interpretation of the references to color in this figure legend, the reader is referred to the web version of this article.)

contrast after passing of the shock wave. In models 1a-b (Fig. 7) we simulate an iron grain embedded in olivine matrices with different porosities. Since iron is only mildly heated by shock, an increase in matrix post-shock temperatures by a higher porosity leads to an increase in the iron grain-matrix temperature contrast and hence more efficient heating of the iron grain. The contrary behavior is observed in models 2a-b, where we simulate a troilite grain embedded in porous olivine matrices. Since shock heating of troilite is generally more efficient than in olivine, an increase of matrix post-shock temperatures by a higher porosity leads to a decreased temperature contrast between troilite grain and matrix. As a consequence, the troilite grain experiences less efficient cooling and overall higher degrees of melting in a highly porous matrix (model 2b), while in a low porosity matrix (model 2a) the troilite grain cools and solidifies within the 3000 µs run time of the model (Fig. 7). Although troilite solidifies in model 2a, a small fraction of troilite continues to melt up to 1000 µs, depicted by the small rise in recorded maximal melt fraction (see beginning of section 3, §2) in Fig. 7.

3.3.2. *Redistribution of heat by diffusion*

The time scales for the relaxation of local temperature contrasts by diffusion depend on the dimensions of the thermal anomalies and hence on the grain sizes within the texture. Consequently, smaller grains experience faster heating or cooling rates than larger grains, given a similar initial temperature contrast. This is apparent in our results for model 1b, a single iron grain in an olivine matrix, where we varied the grain size (see Fig. 8); and for models 5 and 6 (see Figs. 3b-c and 9), where we varied the size of inclusions of weakly shock heated iron in strongly shock heated troilite and vice versa. By looking especially at Fig. 9 where are compiled values for temperatures and melt fractions over time and inclusion size in models 5 and 6, smaller inclusion grains heat (or cool) significantly faster than larger grains and experience higher degrees of melting (or solidification) within the modeled time scales. The surrounding host grains in models 5 and 6 (whose sizes have been held constant) experience stronger temperature changes if they contain larger inclusions, which provide a larger source (or sink) of heat than smaller inclusions. For the grain sizes considered here, heating and cooling rates are in the order of ~0.1–1 K/µs, which implies rapid quenching of molten phases (e.g. troilite inclusions of 50 µm diameter solidify completely within 500 µs). In contrast, iron (both iron inclusions and iron host grains) never cools down or solidifies within the ~500 µs diffusion time simulated in the models, since its thermal evolution during this time period is dominated by heating from the adjacent troilite. In both models 5 and 6 the temperature contrast between the inclusions and the host grain homogenize over time toward equalization.

In addition the grain shapes and textural relations of adjacent grains influence the efficiency of the relaxation of temperature gradients by diffusion. In Fig. 5 we show the results for models 11 and 12 which simulate textures of an albite grain either partially embedded in (model 11) or in contact to (model 12) an underlying larger troilite grain. Both textures are similar but differ both in the size and shape of the albite grain in the size of the shared grain boundary between albite and troilite

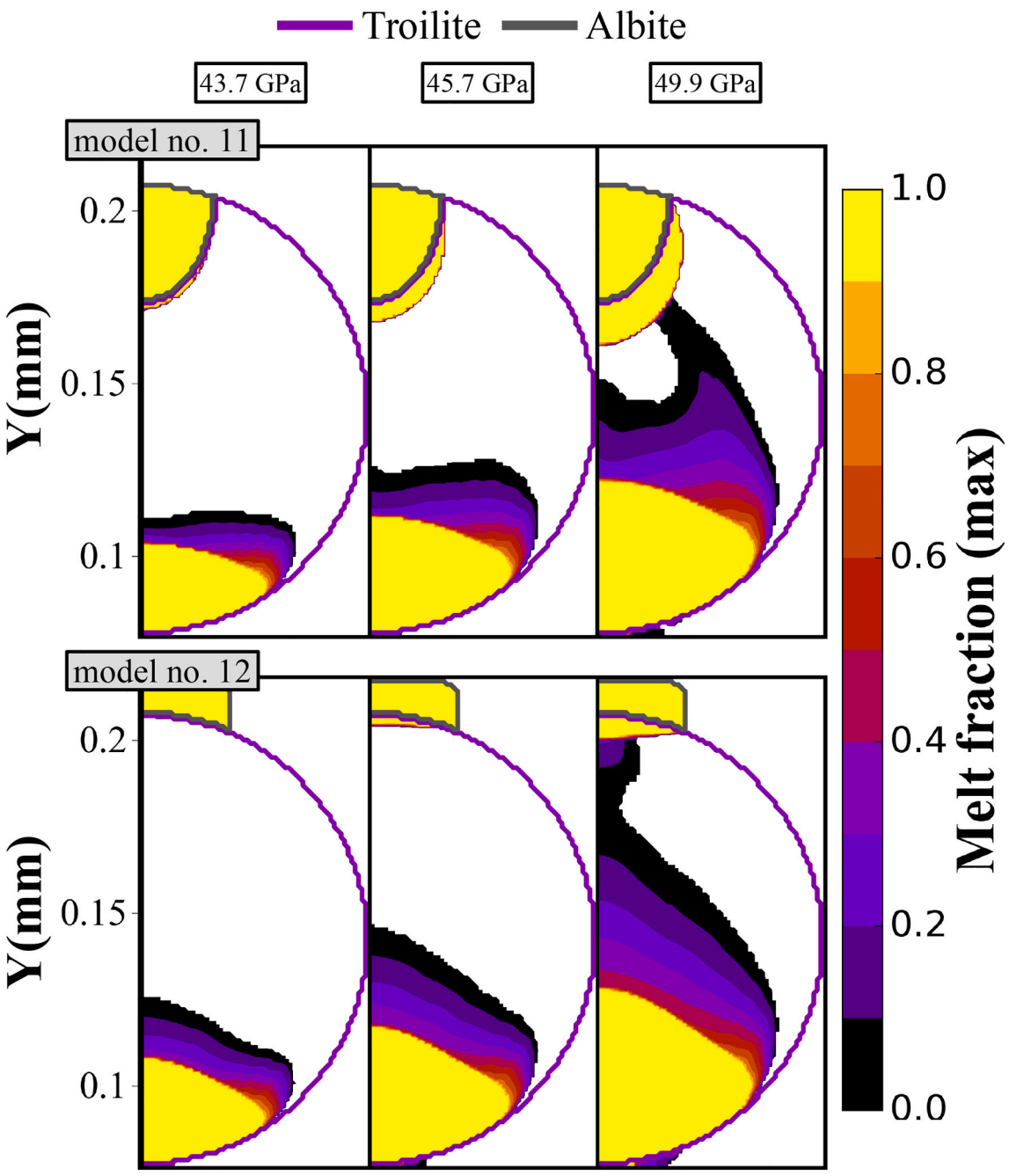

Fig. 5. Effects of nominal shock pressure on the post-shock melting of a troilite grain in contact to albite grains of different shapes (models 11a–c and 12a–c). Individual panels show maximal 2-D melt fraction maps after 3000 μs of heat diffusion. The areas that did not experience any melting are shown in white. (For interpretation of the references to color in this figure legend, the reader is referred to the web version of this article.)

(large shared grain boundary in model 11 and a smaller one in model 12). Its larger grain size allows the albite in model 11 to absorb more shock wave energy than the smaller albite in model 12, which leads to slightly lower degrees of troilite melting at the troilite-albite contact in model 12 compared to model 11. In addition the larger shared grain boundary between albite and troilite in model 11 facilitates a more efficient heat transfer between the phases by diffusion, which also contributes to a higher degree of troilite melting at the contact to albite.

The detailed thermal evolution of model 4e, containing a hemispherical troilite grain on top of a complementarily shaped iron grain in an olivine matrix, is displayed in Fig. 4b. This diagram also illustrates the role of latent heat and the differences in melting temperature among different phases on the temperature distribution in the sample. Where the local melting temperature is reached, any heat added by diffusion is consumed for melting instead of rising the temperature. Hence the temperature profiles contain plateaus corresponding to the melting temperature of the respective phases (i.e. iron-troilite eutectic and olivine). Initially, the troilite grain is completely molten, while the iron grain is initially only partially molten and continues to melt by heat diffusing in from the adjacent phases. Due to the buffering effect of the latent heat, the temperature increase in iron is much lower than the simultaneous temperature decrease in troilite (<200 K vs. > 1000 K in the run time of the model).

3.3.3. *Eutectic melting of intergrown phases*

Iron and troilite can form eutectic mixtures that have significantly

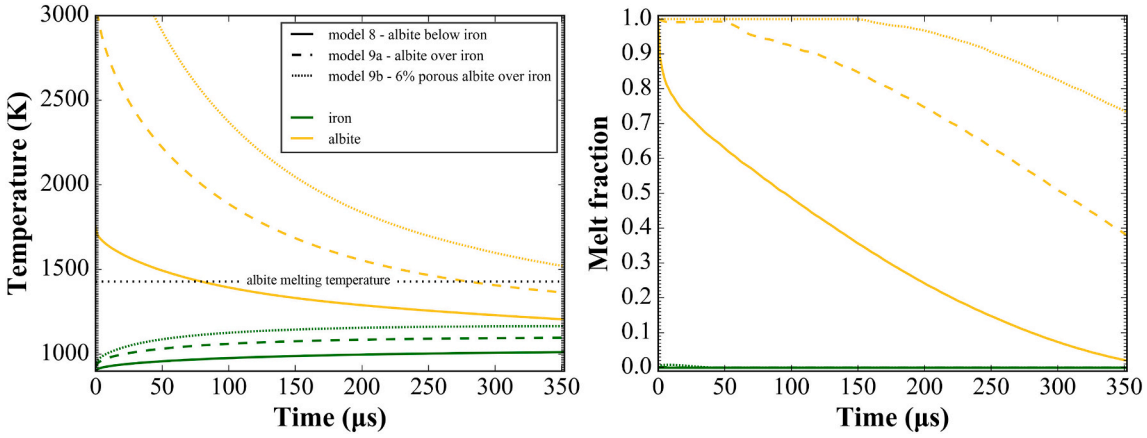

Fig. 6. Evolution of the temperature and melt fraction in adjacent iron and albite grains in textures with different positions and porosities of the albite grains (models 8 and 9a-b). The time is the time passed since the onset of diffusion (i.e. immediately after release of the shock pressure). The temperatures and melt fractions shown for a given phase are average values calculated from all cells occupied by the phase in the 2-D model. (For a colored figure, the reader is referred to the web version of this article.)

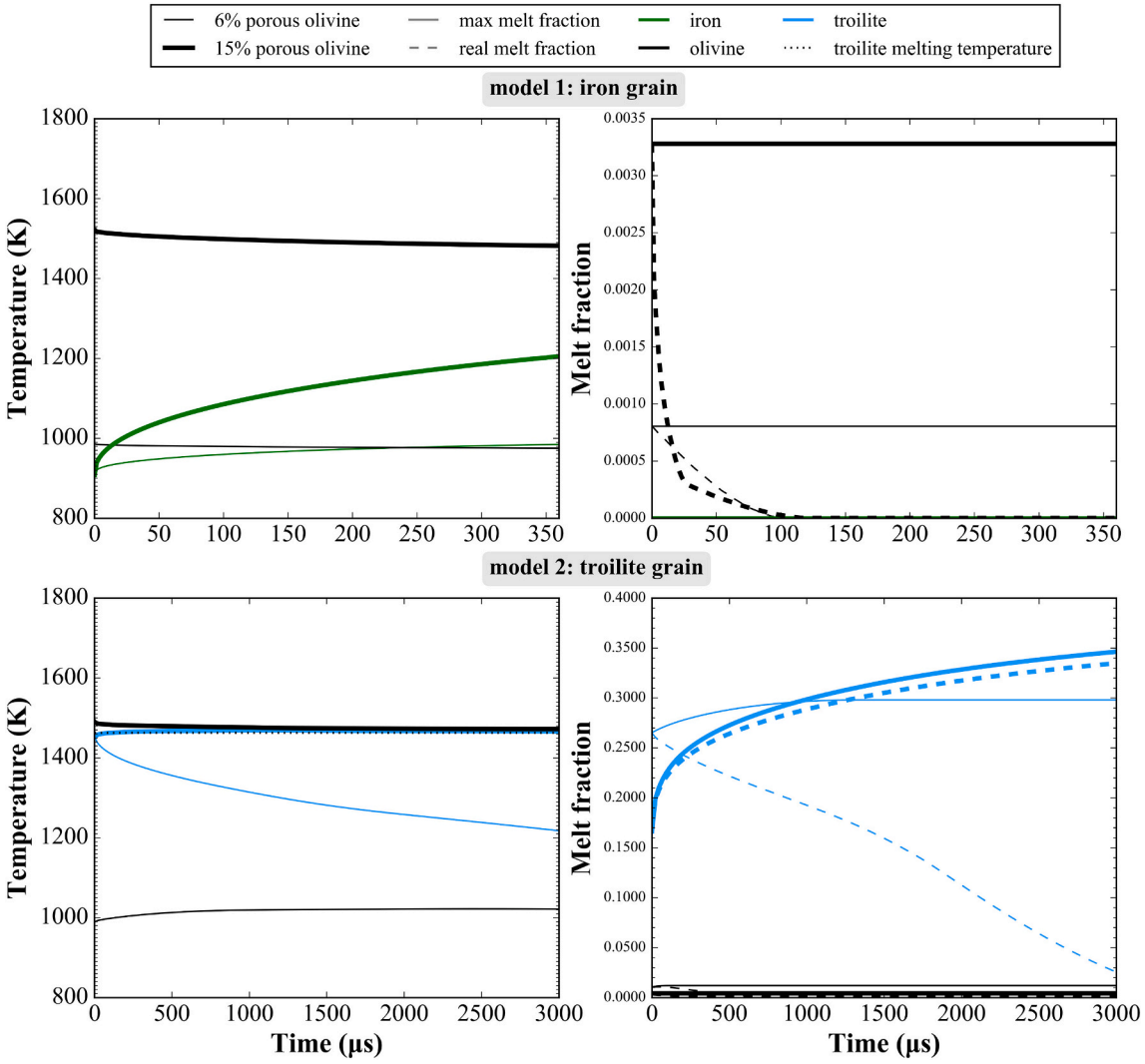

Fig. 7. Evolution of the temperature and melt fraction in iron or troilite grains in olivine matrices (models 1a-b and 2a-b) of different pre-shock porosities (a: 6% porosity, b: 15% porosity). The maximal melt fraction is a cumulative value calculated by adding the maximal melt fractions that have been recorded in each cell of the respective phase up to the time *t*, while the real melt fraction is the current average melt fraction for all cells of the phase at time *t*. The time is the time passed since the onset of diffusion (i.e. immediately after release of the shock pressure). (For a colored figure, the reader is referred to the web version of this article.)

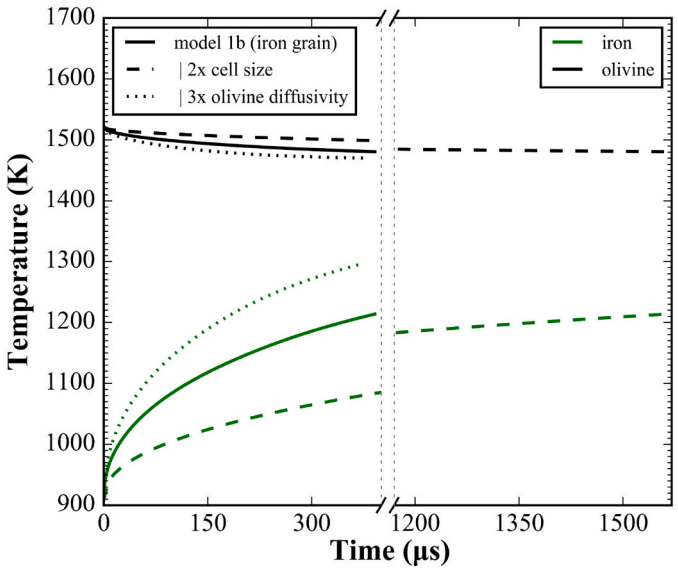

Fig. 8. Temperature as function of diffusion time for model 1b depicting the effects of cell size and olivine thermal diffusivity on iron. Doubling the cell size requires a longer diffusion time, 4× greater, to reach the same variation of temperatures in both phases. Increasing thermal diffusivity in olivine intensifies heating of the iron grain by heat diffusion. The time is the time passed since the onset of diffusion (i.e. immediately after release of the shock pressure). (For a colored figure, the reader is referred to the web version of this article.)

lower melting temperatures than their individual components (1261 K for the eutectic mixture compared to 1811 K for pure iron and 1463 K for pure troilite in our models). Hence iron and troilite will melt more extensively in textures where iron and troilite grains are in direct contact with each other. We assumed such eutectic mixtures of iron and troilite in models 3, 4, 5, 6 and 10 (see Fig. 1 and Table 1). Technically eutectic melting of iron and troilite can initially only occur at the grain boundary. Hence we tend to overestimate the degree of melting by assuming a homogeneous eutectic melting temperature throughout the grains. This effect is illustrated in Fig. 4 (high pressure models 4c-e), where the iron grain experiences melting also on its bottom even though it is not in contact with troilite. In reality this lower part of the iron grain would have a higher melting temperature (corresponding to that of pure iron) and hence experience a lower degree of melting than suggested by the model.

4. Discussion

4.1. Reproduction of OC shock melting features

Observed melting features in shocked ordinary chondrites include iron-troilite veins and intermixed melting of metal and silicates that cannot be explained solely by initial shock heating in the pressure range estimated for the respective chondrites (see *Introduction*). Our results demonstrate that melting of iron metal can potentially be explained by considering diffusion of heat from neighboring phases into the initially only mildly shock heated iron metal, the decrease of its melting temperature in eutectic mixtures with troilite (e.g. Figs. 3, 4), as well as localized heating by increased silicate porosities (e.g. Figs. 7, 10). In the following we discuss which conditions are required to reproduce specific melting features observed in shocked ordinary chondrites, including the formation of plagioclase glass, intermixed melting of metals and silicates and shock-darkening.

4.1.1. Formation of glass and sample cooling rates

The formation of glass from molten plagioclase (Chen and El Goresy, 2000; Yamaguchi and Sekine, 2000; Fritz et al., 2019; Ferrière and Brandstätter, 2015) requires rapid quenching. In our models (8 and 9) the average cooling rate of albite before reaching the solidus can reach several K/µs (~4–6 K/µs, see Fig. 6). These cooling rates are several orders of magnitude faster than the cooling rates required to form silicate glasses (<~0.003 K/µs, (Weinberg et al., 1989), so that our results are generally consistent with the formation of glass by quenching of melt. In shock events, cooling of individual strongly shock heated grains is a two-step process (Stöffler et al., 1991; Tomkins, 2009). Initially, fast cooling at several K/s to 10^6 K/s occurs by relaxing the strong temperature contrasts between individual strongly shock heated grains and the colder matrix at the millimeter scale (Bennett and McSween Jr., 1996; Faure et al., 2003; Miyamoto et al., 2009; Tomkins, 2009; Hu and Sharp, 2017; Baziotis et al., 2018). After temperatures have equilibrated on the grain scale, cooling proceeds at slower rates dependent on the scale of the impact event. In larger natural impacts these cooling rates can reach dimensions similar to thermal metamorphism (e.g. 1–1000 K/Myr, Davison et al., 2012). The cooling rates produced in our models conform with the upper end of the mentioned range of initial cooling rates, which corresponds to small impact events with short shock durations as they are simulated by shock experiments. As we discuss below, longer shock durations can be expected to prolong cooling of shock melts in natural impacts. But since we can expect that glass can still form by melt quenching at cooling rates that are several orders of magnitude slower than those in our models, glass formation by diffusive cooling of shock melt is likely to be a feasible mechanism in large natural impacts.

4.1.2. Intermixed melting

An example of intermixed melting of albite and iron metal is shown in Fig. 10, where we compare the observed intermixed melting in an ordinary chondrite (BSE image by Tomkins, 2009) with our results for models 9a-b, which simulate a similar texture of a ~ 50 µm albite grain intruding into a larger iron grain. We observe that assuming a non-porous albite grain (model 9a) the heating of iron is significantly lower than that observed in the natural chondrite texture. However, assuming an albite grain with 6% porosity increases the local post-shock temperatures sufficiently to induce a degree of iron melting that is very similar to that observed in the chondrite texture (~7% iron metal in the molten region). This result suggests that the mechanisms of local shock pressure concentration by pore crushing in the albite grain and subsequent conductive heating of the neighboring iron are sufficient to explain the observed intermixed melting in the natural sample. However, nominal shock pressures reported for the displayed ordinary chondrite are <40 GPa (Tomkins, 2009), while our model assumes ~50 GPa of nominal shock pressure. In the backscattered electron microscope image in Fig. 10 (Tomkins, 2009) we observe that the troilite grain, in fact, does not melt at contact with iron in the illustrated ordinary chondrite, which is relevant if the shock wave propagates first in the iron grain, then in troilite (Moreau et al., 2018a, model 7). If only metal melts at such low shock pressure, the intermixed melting observed <40 GPa in Tomkins (2009) implies an additional mechanism of pore crushing about the molten metal grain, or a more complex behavior of shock heating in the natural sample, before the diffusion of heat.

Higher degrees of melting could be achieved by varying pre-shock material properties such as silicate porosity or assuming elevated pre-shock temperatures (see section 4.1.4) consistent with the degree of thermal metamorphism experienced by the individual meteorites (Schmitt, 2000; Moreau et al., 2019a). Our models indicate that shock heating of porous silicates can facilitate heating and melting of neighboring initially colder phases (troilite, iron). Increasing the porosity of the olivine matrix to 15% produces olivine post-shock temperatures close to the iron-troilite eutectic melting temperature assuming a nominal shock pressure of 50 GPa (models 1b and 2b, see Table A.1). The porosity in ordinary chondrites can reach up to 30% (Consolmagno et al., 1998), so that eutectic melting is likely to occur also at lower pressures.

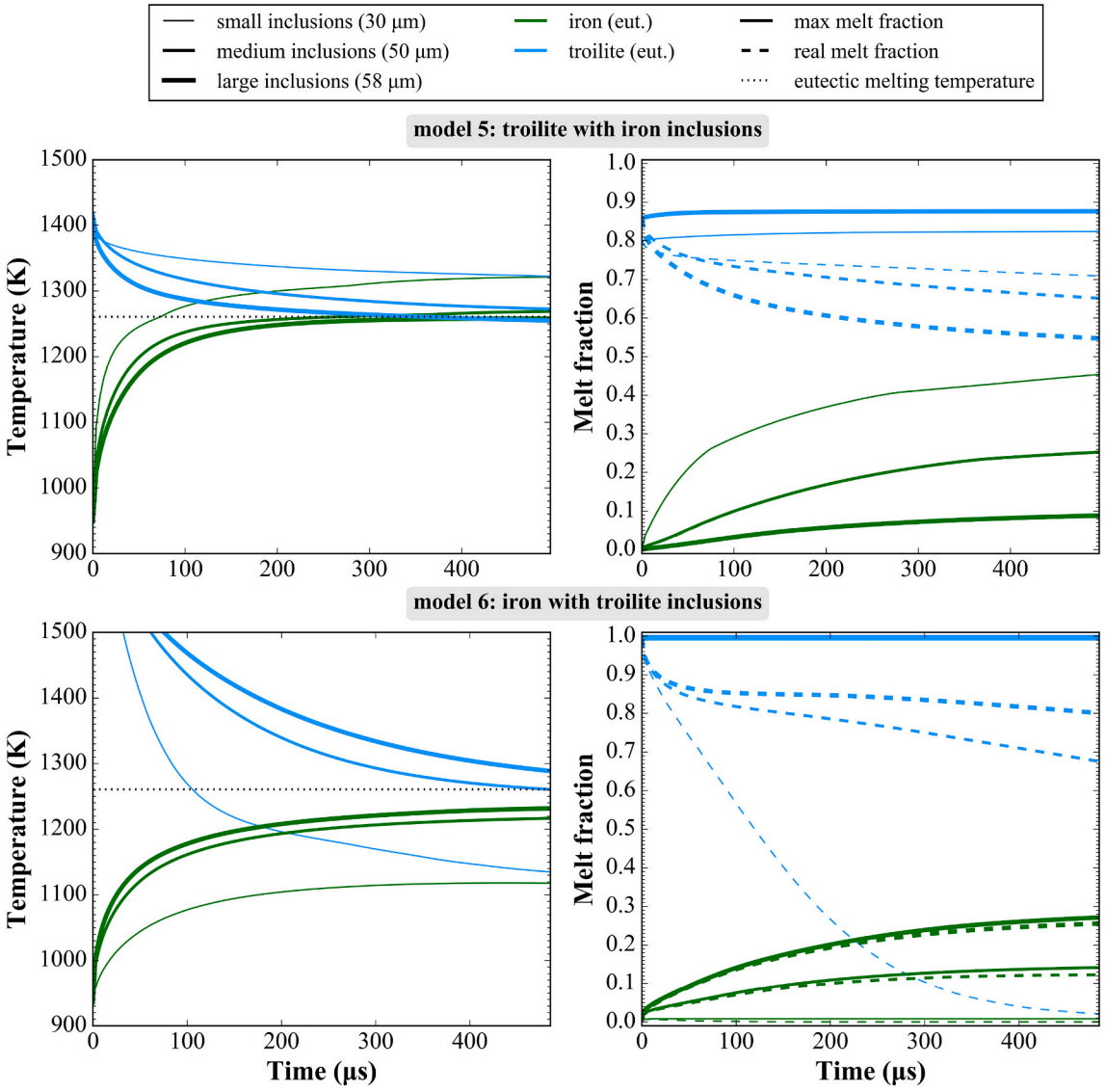

Fig. 9. Influence of inclusion size on the thermal evolution and degree of melting in models 5a–c and 6a–c (with a, b, c corresponding to inclusion sizes of 30 μm, 50 μm and 58 μm diameter, respectively). The black dashed lines in the temperature diagrams represent the eutectic melting temperature for iron and troilite. The maximal melt fraction is a cumulative value calculated by adding the maximal melt fractions that have been recorded in each cell of the respective phase up to the time *t*, while the real melt fraction is the current average melt fraction for all cells of the phase at time *t*. The time is the time passed since the onset of diffusion (i.e. immediately after release of the shock pressure). (For a color figure, the reader is referred to the web version of this article.)

4.1.3. Shock-darkening

The formation of shock-darkening veins in ordinary chondrites (Stöffler et al., 1991) requires both sufficient degrees of metal melting and the migration of this melt into opening cracks in the rock texture.

Shock-darkening is observed over a pressure range of about 40–60 GPa, but in this pressure range shock-darkening may not happen in all cases and the degree of shock-darkening may not strictly correlate with pressure (Bennett and McSween Jr., 1996; Hirata et al., 2009; Kohout et al., 2020; Moreau et al., 2019a). This indicates that shock pressure is not the only factor controlling heating (and hence melting) of iron metals and sulfides, but that it is necessary to consider the textural properties of the material. Since the porosity of silicates in the matrix of the precursor material dictates the degree of shock heating in the matrix (see also Moreau et al., 2019a), chondrites with different initial porosities experience different degrees of heating and melting at the same shock pressures. The degree of melting is not only controlled by local heating but also by the melting temperature of the material, which can be lowered significantly at the contacts between phases that form eutectic mixtures. In our models we considered eutectic melting of intergrown iron metal and troilite grains, but neglected the effects of pressure and the Ni content of the metal phase on eutectic melting temperatures. Metals in ordinary chondrites can contain significant amounts of Ni (Zhang and Fei, 2008; Tomkins, 2009; Mare et al., 2014) and the addition of Ni to a Fe-FeS system has been demonstrated to lower the eutectic melting temperature and affect the heat of fusion of the mixture. Pressure also affects eutectic mixtures and melting temperatures (e.g. decrease of the melting temperature by >200 K at ~10 GPa; Morard et al., 2007; Breuer et al., 2015). The Ni content also varies among the ordinary chondrite types, with Ni contents increasing from H over L to LL. Consequently, melting temperatures and heats of fusion of the FeNi-FeS eutectic mixtures for H-, L- and LL-chondrites are 1236 K, 1223 K, 1181 K and 270.35 kgJ kg^{-1}, 290.95 kgJ kg^{-1}, 294.43 kgJ kg^{-1}, respectively (Mare et al., 2014). To understand how those parameters affect the efficiency of metal melting from shock heating and post-shock heat diffusion in the eutectic mixtures, we replicated the simulation of model 6b using melting temperatures and values for the heats of fusion

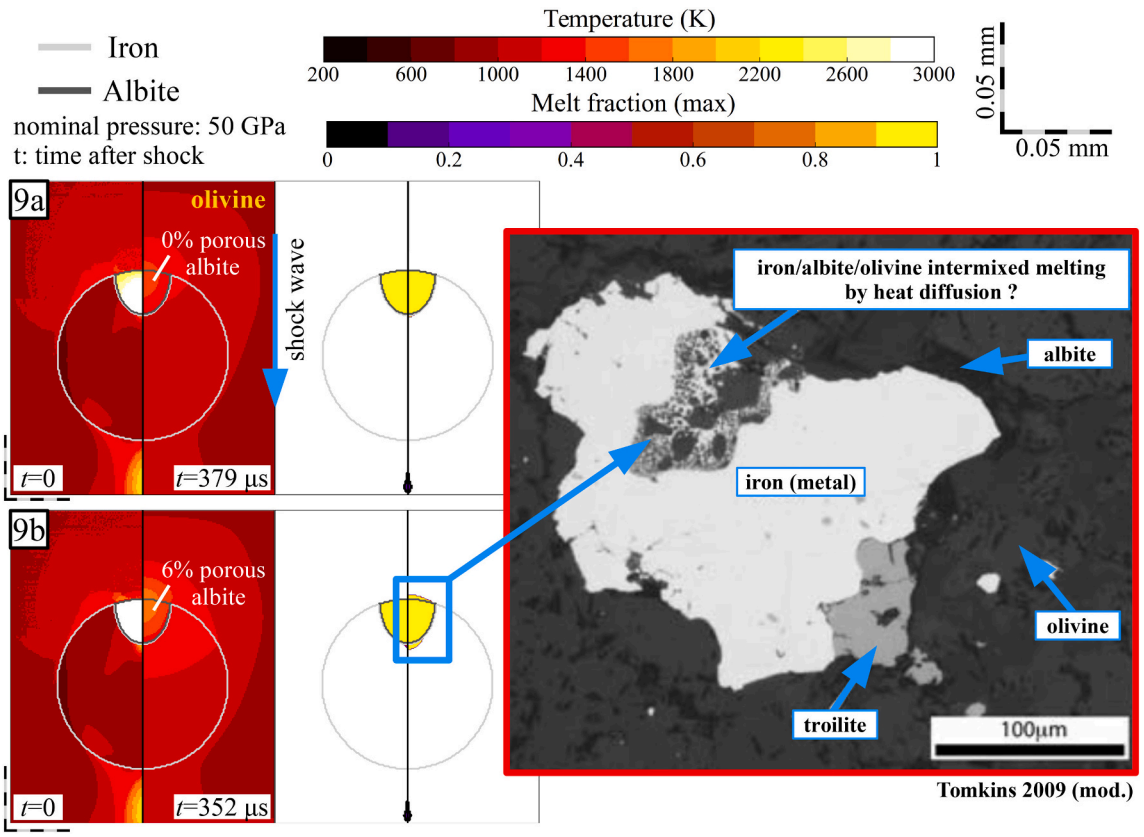

Fig. 10. Intermixed melting of iron and silicates. Left panels display temperature and melt fraction 2 -D maps at different times after the onset of diffusion and for different albite porosities (models 9a–b). The areas that did not experience any melting are shown in white. The backscattered electron microscope image is modified after Tomkins (2009) and illustrates intermixed melting of metals and silicates similar to the results of model 9b. Since the models 9a and 9b were not designed to reproduce the textural details displayed in the backscattered electron microscope image, we can only make a qualitative comparison between observed and modeled melting features. The lack of troilite melting that can be observed in the backscattered electron microscope image is qualitatively consistent with the general observation that albite grains absorb more shock wave energy and hence are more strongly heated by shock than troilite grains (see e.g. models 11c and 12c in Fig. 2). (For interpretation of the references to color in this figure legend, the reader is referred to the web version of this article.)

consistent with the different ordinary chondrite types as listed above. In Fig. 11 we compile the temperature and melt maps (Fig. 11a), the contribution of diffusive melting (Fig. 11b) and progression of temperature and melt fraction over time (Fig. 11c) for the 3 chondrite types. We observe that the resulting shock and diffusive melting for iron does not differ much between H- and L-chondrites because, despite the lower melting temperature in L-chondrites, the L-chondrite eutectic has a higher heat of fusion required to achieve complete melting. In contrast, the degree of melting in LL-chondrites is higher because the LL-chondrite eutectic has a lower melting temperature, but with an otherwise similar heat of fusion to the two other chondrite types. The eutectic melting temperatures used here are based on the average Ni content in the metal. However, individual metal grains in ordinary chondrites are often characterized by an intergrowth of taenite and kamacite. If the shock heating event is rapid enough to cause melting before taenite and kamacite can homogenize, the inhomogeneous distribution of Ni in the grain can lead to a local reduction in the eutectic temperature. At taenite-troilite contacts the eutectic temperature can be as low as 1123 K (Tomkins, 2009), so that locally melting might start earlier than predicted in our models. Though this level of detail is currently not resolved in our model, the effect of chemical inhomogeneity within grains on metal melting and the effect of the shock duration on the degree of taenite-kamacite homogenization during the heating event might be worth investigating in future studies.

An additional requirement for shock-darkening besides sufficient degrees of iron metal and sulfide melting is that the melt stays liquid long enough to penetrate silicate cracks, which requires sufficiently low cooling rates of the molten phases (Tomkins et al., 2013). On the one hand, our results indicate that shock melted troilite can experience fast cooling and solidification if it is surrounded by weakly shock heated phases. In this case iron metal/sulfide melt may solidify before being able to migrate deep enough into opening cracks to constitute a network of veins that is sufficiently large to darken the lithology. On the other hand elevated temperatures of the silicate matrix facilitate longer preservation of molten iron metal and sulfide. However, silicate heating should not be too extensive, otherwise silicate melt films might coat cracks that form during release of the shock and prevent sulfide/metal melt migration (Kohout et al., 2020). As we showed that troilite melts prior to iron (Fig. 9) and because iron sulfides migrates more easily through silicate cracks (since they have better “wetting” properties than iron, Tomkins et al., 2013), our results are in good agreement with the higher abundance of troilite compared to iron in the melt veins of shock-darkened meteorites (Stöffler et al., 1991).

Shock-darkening was reproduced in high pressure shock-recovery experiments with shock pulse durations of <1–4 µs (Schmitt, 2000; Kohout et al., 2020). At such short shock pulse durations, the release of the shock pressure and hence the opening of cracks occurs before the temperature contrasts among adjacent phases have equilibrated by heat diffusion, which can take between a few 100 µs and several ms (see e.g. Fig. 7, where thermal equilibration is not yet reached after 3 ms in some models). This allows molten iron sulfides and metals to penetrate open cracks and form veins before they cool and solidify.

However, the shock pulse durations in shock-recovery experiments of typically <1–4 µs (spherical shocks, Bezaeva et al., 2010, Moreau,

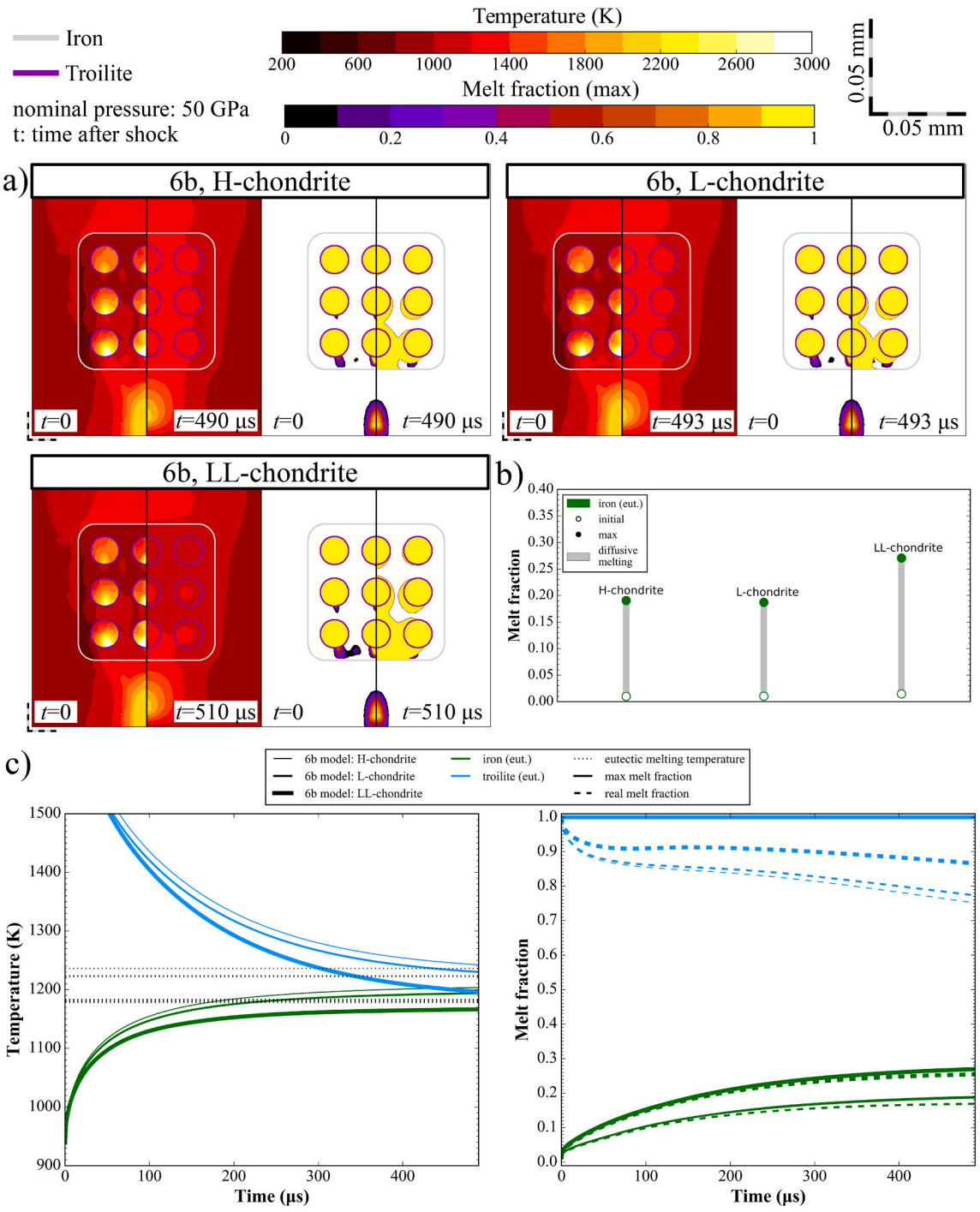

Fig. 11. Differences in the heating and melting behavior of metal-troilite intergrowths (model 6b) between H-, L-, and LL-chondrites due to the effect of different Ni contents in the metal on the eutectic temperature and the heat of fusion of the metal-troilite eutectic mixture (Mare et al., 2014): a) initial and final 2-D temperature maps after ~500 µs of heat diffusion, b) the contribution of heat diffusion to the total melting of iron, c) the evolution of temperature and melt fraction for each model. The melt fraction curves for H- and L-chondrites overlap in c). The areas in a) that did not experience any melting are shown in white. (For interpretation of the references to color in this figure legend, the reader is referred to the web version of this article.)

2019, Kohout et al., 2020; planar shocks, Kowitz et al., 2013; reverberated shocks, Langenhorst and Deutsch, 1994, Langenhorst and Hornemann, 2005, Kohout et al., 2012, Moreau et al., 2018b, Moreau, 2019) are more than 5 orders of magnitude shorter than the shock pulse durations of 100–1000 ms reached during impact processes between asteroids (e.g. Housen and Holsapple, 2003, Cremonese et al., 2012, Moreau, 2019). For the textures simulated in our models, such long shock pulse durations exceed the typical time scales of thermal equilibration on the grain scale, so that some shock melted phases might have solidified before the opening of cracks (e.g. the partially molten troilite grain in model 2a almost solidifies within ~3000 µs, Fig. 7). Hence, longer shock pulse durations can impede the formation of shock-darkening veins, since cracks open only after iron metal and sulfide melts have already re-solidified. Consequently, larger impact events require conditions that preserve iron metal and sulfide melts for longer time scales (i.e. higher post-shock temperatures and/or slower cooling), which can be achieved by higher silicate porosities or higher pre-shock temperatures inside an internally heated asteroid. In any case the

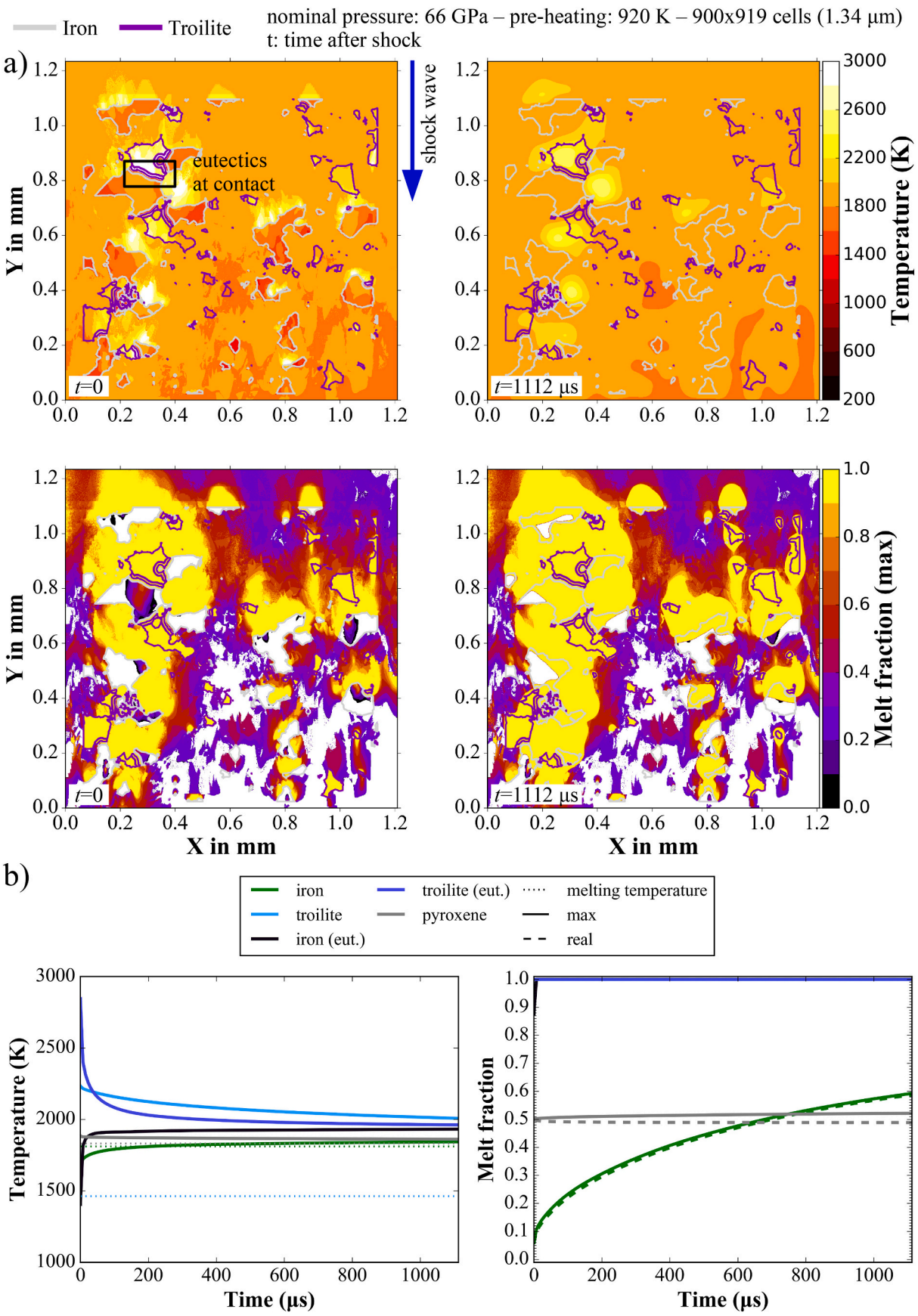

Fig. 12. Shock heating and melting in a preheated enstatite chondrite shocked at 66 GPa (Moreau et al., 2019a, modified): a) initial and final temperature and melt fraction maps after 1112 µs of heat diffusion, b) average temperature and melt fraction as function of diffusion time for individual phases. The areas in a) that did not experience any melting are shown in white. (For interpretation of the references to color in this figure legend, the reader is referred to the web version of this article.)

dependence of the required conditions for shock-darkening on the shock pulse duration implies that the results of shock recovery experiments cannot be readily transferred to the shock metamorphism resulting from collisions between asteroids.

4.1.4. Shock melting in naturally or experimentally shocked pre-heated chondrites

Moreau et al. (2019a) used iSALE to produce detailed post-shock heating and melting maps of complex textures that were modeled after backscattered electron microscope images of ordinary and enstatite chondrites to allow a direct comparison with experimental results. Among other numerical models, Moreau et al. (2019a) attempted to reproduce the results of a shock-recovery experiment by Schmitt (2000), where an H chondrite with 10% porosity was preheated to 920 K and experimentally shocked at 60 GPa, which resulted in a total melt fraction of 0.35. However, the melt fraction predicted by the model of Moreau et al. (2019a) for these experimental conditions was only 0.09.

One possible reason for this discrepancy is that in the model all silicate phases were assumed to be olivine, which neglected the presence of silicates like plagioclase and pyroxene that have lower melting temperatures and are generally more strongly heated by shock than olivine. Another reason the melt fraction was underestimated is that post-shock heat diffusion was not considered. As we have demonstrated in this work, post-shock heat diffusion has an especially high impact on the melt fractions of phases like iron metal that experience only weak initial shock heating. In the study of Moreau et al. (2019a) the melting of pure iron metal was rarely observed, even in models that yielded high degrees of silicate melting and initial conditions such as pre-heated chondrites.

To further study the extent of melting in preheated materials and the importance of heat diffusion for this process, we adapted the simpler model N1 from Moreau et al. (2019a), which reproduces the texture of the enstatite chondrite Neuschwanstein. Since the silicate portion of enstatite chondrites is dominated by pyroxene, we assumed pyroxene instead of olivine as composition of the silicate matrix of the model. To make sure that the results are not affected by the boundary conditions of the diffusion code (see *Methods*), we assumed a rim of pure pyroxene around the original texture. Other model parameters, including silicate porosity (10%) and nominal shock pressure (66 GPa), were left unchanged. We also kept the assumption that eutectic melting occurs within a distance of 10 μm from iron-troilite grain boundaries (Moreau et al., 2019a).

The results of our model are summarized in Fig. 12 and Table A.1. As expected, melting of iron by initial shock heating is rare. However, substantial iron heating and melting is observed after simulating diffusion of heat from strongly shock heated adjacent troilite or pyroxene into the cooler iron grains (see right panels in Fig. 12a). The melt fraction in pure iron rose from 0.06 immediately after shock to 0.59 after ~1 ms of diffusion, with more than half of all iron grains in the texture melting solely by heat diffusion. These results indicate that heat diffusion is the major cause for shock melting of pure iron metal in ordinary chondrites which experienced very high shock pressures by high energy impacts at preheated conditions (i.e. due to radiogenic heating on their parent bodies). The total melt fraction in the enstatite chondrite model is initially 0.49 and increases to 0.56 by subsequent heat diffusion. These results also demonstrate that conducting numerical shock experiments and comparing them to real experiments asks to consider many contributing factors: a correct representation of the target texture (considering all present silicate phases and their grain sizes and shapes), the shock conditions (like shock pressure and shock wave direction) and the heating and melting of metals by diffusion.

4.2. Model limitations and possible improvements

4.2.1. Deformation and porosity

Our results demonstrate that localized heating by pore crushing is an important mechanism for the formation and preservation of shock melts. However, pore collapse is associated with strong deformations, which requires an explicit transfer of local material properties from the deformed iSALE mesh to the diffusion code to obtain reliable results. The current version of the code does not yet include an interpolation algorithm to make such a transfer, so that we are limited to model setups producing limited degrees of deformation. Since our results indicate that pore crushing might play a major role in the localized heating required for the formation of shock-darkening veins, this is a feature that will be implemented in future versions of the code.

Heating from pore collapse is strongly dependent on the pore shape and the orientation of the pore relative to the direction of the shock wave and hence plays an important role in the formation of melt veins (Levesque and Vitello, 2015; Moreau et al., 2017, 2019a). Collapse of elongated pores oblique to the shock wave direction generates higher temperatures than collapse of pores oriented longitudinally or transversely to the shock wave (Moreau et al., 2019a). Porosity is also an important parameter influencing the post-shock properties of the material, since cracks and pores can form during release of the shock pressure. This post-shock porosity is not only important for the formation of shock veins but also influences the thermal conductivity of the material (Shabbir et al., 2000) and hence the relaxation of post-shock temperature contrasts by diffusion.

4.2.2. Heat diffusion and melting during shock

As discussed above, our current model setup is designed to simulate shock events with short shock pulse durations, where diffusion occurs after the shock wave has subsided. This approach allows us to reproduce the conditions in shock experiments, but is not suitable for the simulation of larger impact events with longer shock pulse durations. In large impacts, shock pulse durations are long enough that temperature contrasts on the grain scale are significantly affected by heat diffusion before the shock wave has subsided. In this case we need to explicitly consider the pressure and temperature changes during passing of the shock wave and their effects on the thermal diffusivities of the material. On a technical level this requires the direct implementation of a heat diffusion module into the iSALE code, rather than simulating diffusion in a separate post-processing step, and the consideration of the pressure dependence of thermal diffusivities, which is currently not implemented in the diffusion model.

Thermal diffusivities of metals and silicates generally decrease with increasing temperature and increase with increasing pressure (e.g. iron, Konôpková et al., 2016, or olivine, Osako et al., 2004). During passing of the shock wave local temperatures are higher than the local post-shock temperatures (e.g. in-shock temperatures are $> \sim$ 100–300 K higher than post-shock temperatures in olivine for peak shock pressures of 50–100 GPa, Moreau et al., 2017, 2018a, 2019a). However, the lowering effect of this temperature increase on the thermal diffusivity is counteracted by the stronger diffusivity enhancing effect of increased pressures.

To estimate the thermal diffusivity of olivine at conditions relevant for shock-darkening, we used the pressure dependence determined by Osako et al. (2004) for pressures up to 8.3 GPa to extrapolate olivine thermal diffusivities to a pressure of 50 GPa. The resulting olivine thermal diffusivities are ~3–4 times higher than those at 0 GPa. To study the effects of such a change in olivine thermal diffusivity, we repeated the simulation of model 1b with a 3 times higher thermal diffusivity in olivine. As a result of the increased olivine thermal diffusivity the iron grain embedded in the olivine matrix experiences significantly stronger heating (Fig. 8). This suggests that increased thermal diffusivities during shock might increase the degree of heating and melting of iron metal and sulfides that is required for the formation of shock-darkening veins.

However, to evaluate the effect of in-shock diffusion on the degree of iron metal and iron sulfide melting we also need to consider the pressure dependence of the melting temperature of the respective phases. Melting temperatures generally increase with increasing pressure. At 50 GPa troilite melts only at ~3000 K (Williams and Jeanloz, 1990), which is

significantly higher than the troilite melting temperature of 1463 K at 0 GPa and also exceeds the temperatures of <2000 K reached during shock (Moreau et al., 2019a), so that troilite can be expected to melt only after the peak pressure is reached and pressures have begun to decrease.

These complexities make it difficult to estimate a net effect of diffusion during shock events with longer shock pulse durations without explicitly modeling the system. Therefore further study is required to investigate the melting behavior of chondrite textures during shock events with long shock pulse durations.

5. Conclusions

We have investigated the role of post-shock heat diffusion for heating and melting of individual phases (silicates, iron sulfides, and metals) in chondrite textures by modeling shock heating and subsequent redistribution of heat by diffusion. We demonstrate that modeling heat diffusion on the grain scale is essential to understand melting features in shock experiments, and naturally shocked chondrites, and to investigate the role of different textural features and external conditions for the observed degree of melting. We find that:

a) Metallic iron does not melt primarily by shock heating but by diffusion of heat from adjacent, strongly shock heated phases. This explains several aspects of the melting behavior of iron metal observed in shocked ordinary chondrites, including the lack of a distinct correlation between shock pressure and degree of iron melting, and localized melting of iron metal depending on the textural context (i.e. type of adjacent phases, eutectic mixtures).
b) Pore crushing is an important mechanism for the absorption of shock wave energy and hence has a major influence on local post-shock temperatures. Therefore silicate porosity is a crucial factor controlling local rates of heating and cooling, degrees of melting, and the duration of melt preservation.
c) Intermixed melting of iron metal and silicates results from shock heating of silicates and subsequent heating and melting of adjacent iron metal by diffusion.
d) The formation of shock-darkening veins requires 1) extensive melting of iron metal and/or iron sulfides and 2) the simultaneous presence of open cracks, which form only during release of the shock pressure. Consequently, the extent of shock-darkening depends on multiple factors that control the post-shock temperature (i.e. shock pressure, porosity, pre-shock temperature) and the relative dimensions of the shock pulse duration (dependent on the type of shock event) and the duration of melt preservation (dependent on local cooling and solidification rates, ergo shapes and sizes of grains, and local temperature contrasts).
e) The duration of the shock pulse determines if the relaxation of temperature contrasts between adjacent grains by heat diffusion occurs mainly during shock or after the shock wave has subsided. Since elevated pressures affect the thermal diffusivities and melting temperatures of the shocked phases, the required conditions for shock-darkening (and shock melting in general) are different in shock experiments and natural impacts. Our modeling approach is suitable to simulate shock events with short shock pulse durations and can hence be used to reproduce shock features produced in shock experiments. Modeling of shock features produced by larger impact events with longer shock pulse duration requires the simulation of heat diffusion during shock and respective modifications in the modeling approach.

Funding

This work was supported by the Academy of Finland Project no. 293975, by the European Regional Development Fund and the programme Mobilitas Pluss (Grant No. MOBJD639), and funded by the Deutsche Forschungsgemeinschaft (DFG, German Research Foundation) – Project-ID 263649064 – TRR 170. This is TRR 170 Publication No. 121.

CRediT authorship contribution statement

Juulia-Gabrielle Moreau: Conceptualization, Methodology, Software, Validation, Formal analysis, Investigation, Resources, Data Curation, Writing - Original Draft, Writing - Review & Editing, Visualization, Supervision, Funding acquisition **Sabrina Schwinger**: Conceptualization, Methodology, Writing - Review & Editing, Visualization, Funding acquisition.

None.

Acknowledgements

We gratefully acknowledge the developers of iSALE-2D, including Gareth Collins, Kai Wünnemann, Dirk Elbeshausen, Boris Ivanov and Jay Melosh. This work used the pySALEPlot tool written by Tom Davison for treating iSALE models. The iSALE-Dellen version was used in this work (Collins et al., 2016) with modifications from Moreau et al. (2019a, 2019b) and the script for treating the iSALE models are similar to those from Moreau et al. (2019b). We also thank Lars Kaislaniemi for having shared the idea for the diffusion code.

Appendix. Supplementary data

Supplementary data to this article can be found online at https://doi.org/10.17632/8cp735rjdh.1.

References

Abu-Eishah, S.I., 2001. Correlations for the thermal conductivity of metals as a function of temperature. Int. J. Thermophys. 22 (6), 1855–1868. https://doi.org/10.1023/A:1013155404019.
Ahrens, T.J., Holland, K.G., Chen, G.Q., 1998. Shock temperatures and the melting point of iron. In: Schmidt, S.C., Dandekar, D.P., Forbes, J.W. (Eds.), Shock Compression of Condensed Matter. Woodbuty, AIP Press, New York, pp. 133–136.
Amsden A. A., Ruppel H. M. and Hirt C. W. (1980) SALE: a simplified ALE computer program for fluid flow at all speeds. *Los Alamos National Laboratories Report* LA-8095, los Alamos, New Mexico. doi:https://doi.org/10.2172/5176006.
Baziotis, I, Asimow, P.D., Hu, J., Ferrière, L, Ma, C., Cernok, A., Anand, M., Topa, D., 2018. High pressure minerals in the Château-Renard (L6) ordinary chondrite: implications for collisions on its parent body. Sci. Rep. 8, 9851. https://doi.org/10.1038/s41598-018-28191-6.
Bennett, M.E., McSween Jr., H.Y., 1996. Shock features in iron-nickel metal and troilite of L-group ordinary chondrites. Meteorit. Planet. Sci. 31, 255–264. https://doi.org/10.1111/j.1945-5100.1996.tb02021.x.
Bezaeva, N.S., Badjukov, D.D., Rochette, P., Gattacceca, J., Trukhin, V.I., Kozlov, E.A., Uehara, M., 2010. Experimental shock metamorphism of the L4 ordinary chondrite Saratov induced by spherical shock waves up to 400 GPa. Meteorit. Planet. Sci. 45, 1007–1020. https://doi.org/10.1111/j.1945-5100.2010.01069.x.
Bischoff, A., Schleiting, M., Patzek, M., 2018. Shock stage distribution of 2280 ordinary chondrites—can bulk chondrites with a shock stage of S6 exist as individual rocks? Meteorit. Planet. Sci. 54 (10), 2189–2202. https://doi.org/10.1111/maps.13208.
Bland, P.A., Collins, G.S., Davison, T.M., Abreu, N.M., Ciesla, F.J., Muxworthy, A.R., Moore, J., 2014. Pressure-temperature evolution of primordial solar system solids during impact-induced compaction. Nat. Commun. 5, 5451. https://doi.org/10.1038/ncomms6451.
Branlund, J.M., Hofmeister, A.M., 2012. Heat transfer in plagioclase feldspars. Am. Mineral. 97, 1145–1154. https://doi.org/10.2138/am.2012.3968.
Breuer, D., Rueckriemen, T., Spohn, T., 2015. Iron snow, crystal floats, and inner-core growth: modes of core solidification and implications for dynamos in terrestrial planets and moons. Prog. Earth Planet. Sci. 2 (39), 26–1180. https://doi.org/10.1186/s40645-015-0069-y.
Britt, D.T., Consolmagno, S.J., 2003. Stony meteorite porosities and densities: a review of the data through 2001. Meteorit. Planet. Sci. 38 (8), 1161–1180. https://doi.org/10.1111/j.1945-5100.2003.tb00305.x.
Britt, D.T., Pieters, C.M., 1989. Bidirectional reflectance characteristics of black chondrite meteorites (abstract). In: 20th Lunar and Planetary Science Conference. Houston, Texas, pp. 109–110.
Britt, D.T., Pieters, C.M., 1994. Darkening in black and gas-rich ordinary chondrites: the spectral effects of opaque morphology and distribution. Geochim. Cosmochim. Acta 58, 3905–3919. https://doi.org/10.1016/0016-7037(94)90370-0.

Britt, D.T., Pieters, C.M., Petaev, M.I., Zaslavskaya, N.I., 1989. The Tsarev meteorite - petrology and bidirectional reflectance spectra of a shock-blackened L chondrite. In: 19th Lunar and Planetary Science Conference. Houston, Texas, pp. 537–545.
Chase Jr., M.W., 1998. NIST-JANAF thermochemical tables, 4th edition, *J. Phys. Chem. Ref.* Data, monograph 9, 1–1951.
Chen, M., El Goresy, A., 2000. The nature of maskelynite in shocked meteorites: not diaplectic glass but a glass quenched from shock-induced dense melt at high pressures. Earth Planet. Sci. Lett. 179, 489–502. https://doi.org/10.1016/S0012-821X(00)00130-8.
Chen, M., Xie, X., Wang, D., Wang, S., 2002. Metal-troilite-magnetite assemblage in shock veins of Sixiangkou meteorite. Geochim. Cosmochim. Acta 66 (17), 3143–3149.
Collins, G.S., Melosh, H.J., Ivanov, B.A., 2004. Modeling damage and deformation in impact simulations. Meteorit. Planet. Sci. 39, 217–231. https://doi.org/10.1111/j.1945-5100.2004.tb00337.x.
Collins, G.S., Melosh, H.J., Wünnemann, K., 2011. Improvements to the ε-α porous compaction model for simulating impacts into high-porosity solar system objects. Int. J. Impact Eng. 38, 434–439. https://doi.org/10.1016/j.ijimpeng.2010.10.013.
Collins G. S., Elbeshausen D., Wünnemann K., Davison T. M., Ivanov B. and Melosh H. J. (2016) iSALE-Dellen manual: a multi-material, multi-rheology shock physics code for simulating impact phenomena in two and three dimensions. doi:https://doi.org/10.6084/m9.figshare.3473690.
Consolmagno, G.J., Britt, D.T., Stoll, C.P., 1998. The porosities of ordinary chondrites: models and interpretation. Meteorit. Planet. Sci. 33, 1221–1229. https://doi.org/10.1111/j.1945-5100.1998.tb01307.x.
Consolmagno, G.J., Britt, D.T., Macke, R.J., 2008. The significance of meteorite density and porosity. Chem. Erde 68, 1–29. https://doi.org/10.1016/j.chemer.2008.01.003.
Cremonese, G., Martellato, E., Marzari, F., Kuhrt, E., Scholten, F., Preusker, F., Wünnemann, K., Borin, P., Massironi, M., Simioni, E., Ip, W., the OSIRIS team, 2012. Hydrocode simulations of the largest crater on asteroid Lutetia. Planet. Space Sci. 66, 147–154. https://doi.org/10.1016/j.pss.2012.01.001.
Davison, T.M., Ciesla, F.J., Collins, G.S., 2012. Post-impact thermal evolution of porous planetesimals. Geochim. et Cosmochim. Acta 95, 252–269.
Davison T. M., Collins G. S. and Bland P. A. (2016) Mesoscale modeling of impact compaction of primitive solar system solids. Astrophys. J. 821, 17 pp. doi:https://doi.org/10.3847/0004-637X/821/1/68.
Davison, T.M., Derrick, J.G., Collins, G.S., Bland, P.A., Rutherford, M.E., Chapman, D.J., Eakins, D.E., 2017. Impact-induced compaction of primitive solar system solids: the need for mesoscale modelling and experiments. Procedia Eng. 204, 405–412. https://doi.org/10.1016/j.proeng.2017.09.801.
DeMeo, F.E., Carry, B., 2014. Solar system evolution from compositional mapping of the asteroid belt. Nature 505, 629–634.
DeMeo, F.E., Binzel, R.P., Slivan, S.M., Bus, S.J., 2009. An extension of the Bus asteroid taxonomy into the near-infrared. Icarus 202, 160–180. https://doi.org/10.1016/j.icarus.2009.02.005.
Ebert, M., Kowitz, A., Schmitt, R.T., Reimold, W.U., Mansfeld, U., Langenhorst, F., 2018. Localized shock-induced melting of sandstone at low shock pressures (<17.5 GPa): an experimental study. *Meteorit. Planet.* Sci. 53 (8), 1633–1643. https://doi.org/10.1111/maps.12948.
Faure, F., Trolliard, G., Nicollet, C., Montel, J.-M., 2003. A developmental model of olivine morphology as a function of the cooling rate and the degree of undercooling. Contrib. Mineral. Petrol. 145, 251–263. https://doi.org/10.1007/s00410-003-0449-y.
Ferrière L. and Brandstätter F. (2015) What is maskelynite? Back to the original description and thin sections in which it was first described, in: *78th Annual Meeting of the Meteoritical Society*, abstract no. 5184.
Fritz, J., Greshake, A., Fernandes, V.A., 2017. Revising the shock classification of meteorites. Meteorit. Planet. Sci. 52, 1216–1232. https://doi.org/10.1111/maps.12845.
Fritz, F., Fernandes, V.A., Greshake, A., Holzwarth, A., Bottger, U., 2019. On the formation of diaplectic glass: shock and thermal experiments with plagioclase of different chemical compositions. Meteorit. Planet. Sci. 54 (7), 1533–1547. https://doi.org/10.1111/maps.13289.
Gibert, B., Schilling, F.R., Gratz, K., Tommasi, A., 2005. Thermal diffusivity of olivine single crystals and a dunite at high temperature: evidence for heat transfer by radiation in the upper mantle. Phys. Earth Planet. Inter. 151, 129–141. https://doi.org/10.1016/j.pepi.2005.02.003.
Güldemeister, N., Wünnemann, K., Durr, N., Hiermaier, S., 2013. Propagation of impact-induced shock waves in porous sandstone using mesoscale modeling. Meteorit. Planet. Sci. 48, 115–133. https://doi.org/10.1111/j.1945-5100.2012.01430.x.
Heymann, D., 1967. On the origin of hypersthene chondrites: ages and shock effects of black chondrites. Icarus 6, 189–221. https://doi.org/10.1016/0019-1035(67)90017-6.
Hirata, N., Kurita, K., Sekine, T., 2009. Simulation experiments for shocked primitive materials in the solar system. Physc. Earth. Planet. Inter. 174, 227–241. https://doi.org/10.1016/j.pepi.2008.09.016.
Hofmeister, A.M., 2012. Thermal diffusivity of orthypyroxenes and protoenstatite as a function of temperature and chemical composition. Eur. J. Mineral. 24, 669–681. https://doi.org/10.1127/0935-1221/2012/0024-2204.
Horstmann, M., Humayun, M., Harries, D., Langenhorst, F., Chabot, N.L., Bischoff, A., Zolensky, M.E., 2013. Wüstite in the fusion crust of Almahata Sitta sulfide-metal assemblage MS-166: evidence for oxygen in metallic melts. Meteorit. Planet. Sci. 48 (5), 730–743.
Housen, K.R., Holsapple, K.A., 2003. Impact cratering on porous asteroids. Icarus 163, 102.119.
Hu, H., Argyropoulos, S.A., 1996. Mathematical modelling of solidification and melting: a review. Modelling Simul. Mater. Sci. Eng. 4, 371–396.
Hu, J., Sharp, T.G., 2017. Back-transformation of high-pressure minerals in shocked chondrites: low-pressure mineral evidence for strong shock. Geochim. Cosmochim. Acta 215, 277–294. https://doi.org/10.1016/j.gca.2017.07.018.
Hwang, H., Galtier, E., Cynn, H., Eom, I., Chun, S.H., Bang, Y., Hwang, G.C., Choi, J., Kim, T., Kong, M., Kwon, S., Kang, K., Lee, H.J., Park, C., Lee, J.I., Lee, Y., Yang, W., Shim, S.-H., Vogt, T., Kim, S., Park, J., Kim, S., NamLee, D., Hyun, H., Kim, M., Koo, T.-Y., Kao, C.-C, SekineLee, T.Y., 2020. Subnanosecond phase transition dynamics in laser-shocked iron. Sci. Adv. 6, eaaz5132.
Ivanov, B.A., Deniem, D., Neukum, G., 1997. Implementation of dynamic strength models into 2D hydrocodes: applications for atmospheric breakup and impact cratering. Int. J. Impact Eng. 20, 411–430. https://doi.org/10.1016/S0734-743X(97)87511-2.
Jaret, S.J., Woerner, W.R., Phillips, B.L., Ehm, L., Nekvasil, H., Wright, S.P., Glotch, T.D., 2015. Maskelynite formation via solid-state transformation: evidence of infrared and X-ray anisotropy. *J. Geophys. Res.* E Planets 120, 570–587. https://doi.org/10.1002/2014JE004764.
Keil, K., Bell, J.F., Britt, D.T., 1992. Reflection spectra of shocked ordinary chondrites and their relationship to asteroids. Icarus 98, 43–53. https://doi.org/10.1016/0019-1035(92)90205-L.
Kohout, T., Pesonen, L.J., Deutsch, A., Wünnemann, K., Nowka, D., Hornemann, U., Heikinheimo, E., 2012. Shock experiments in range of 10-45 GPa with small multidomain magnetite in porous targets. Meteorit. Planet. Sci. 47 (10), 1671–1680. https://doi.org/10.1111/maps.12003.
Kohout, T., Gritsevich, M., Grokhovsky, V.I., Yakovlev, G.A., Haloda, J., Halodova, P., Michallik, R.M., Penttilä, A., Muinonen, K., 2014. Mineralogy, reflectance spectra, and physical properties of the Chelyabinsk LL5 chondrite - insight into shock-induced changes in asteroid regoliths. Icarus 228, 78–85. https://doi.org/10.1016/j.icarus.2013.09.027.
Kohout, T., Petrova, E.V., Yakovlev, G.A., Grokhovsky, V.I., Penttilä, A., Maturilli, A., Moreau, J.-G., Berzin, S.V., Wasiljeff, J., Danilenko, I.A., Zamyatin, D.A., Muftakhetdinova, R.F., Heikkilä, M., 2020. Experimental constraints on the ordinary chondrite shock darkening caused by asteroid collisions. Astron. Astrophys. 639, A146.
Konôpková Z., McWilliams R. S., Gómez-Pérez N. and Goncharov A. F. (2016) Direct measurement of thermal conductivity in solid iron at planetary core conditions. Nature 534, 99–101.https://doi:10.1038/nature18009.
Kowitz, A., Schmitt, R.T., Reimold, W.U., Hornemann, U., 2013. The first MEMIN shock recovery experiments at low shock pressure (5-12.5 GPa) with dry, porous sandstone. *Meteorit. Planet.* Sci. 48 (1), 99–114. https://doi.org/10.1111/maps.12030.
Kraus, R.G., Stewart, S.T., Swift, D.C., Bolme, C.A., Smith, R.F., Hamel, S., Hammel, B.D., Spaulding, D.K., Hicks, D.G., Eggert, J.H., Collins, G.W., 2012. Shock vaporization of silicate and the thermodynamics of planetary impact events. J. Gephys. Res. 117, E09009 https://doi.org/10.1029/2012JE004082.
Langenhorst, F., Deutsch, A., 1994. Shock experiments on pre-heated alpha-quartz and beta-quartz: I. Optical and density data. *Earth Planet. Sci. Lett.* 125, 407–420. https://doi.org/10.1016/0012-821x(94)90229-1.
Langenhorst, F., Hornemann, U., 2005. Shock experiments on minerals: basic physics and techniques. EMU Notes Mineral. 7, 357–387.
Lehner, S.W., Buseck, P.R., McDonough, W.F., 2010. Origin of kamacite, schreibersite, and perryite in metal-sulfide nodules of the enstatite chondrite Sahara 97072 (EH3) *Meteorit.* Planet. Sci. 45 (2), 289–303.
Levesque, G.A., Vitello, P., 2015. The effect of pore morphology on hot spot temperature. Propellants Explos. Pyrotech. 40, 303–308.
Luo, S.-N., Ahrens, T.J., Asimow, P.D., 2003. Polymorphism, superheating, and amorphization of silica upon shock wave loading and release. J. Geophys. Res. 108 (B9), 2421. https://doi.org/10.1029/2002JB002317.
Mare, E.R., Tomkins, A.G., Godel, B.M., 2014. Restriction of parent body heating by metal-troilite melting: thermal models for the ordinary chondrites. Meteorit. Planet. Sci. 49, 636–651. https://doi.org/10.1111/maps.12280.
Melosh, H.J.J., Ryan, E.V.V., Asphaug, E., 1992. Dynamic fragmentation in impacts: Hydrocode simulation of laboratory impacts. J. Geophys. Res. 97, 14735–14759. https://doi.org/10.1029/92JE01632.
Miyamoto, M., Mikouchi, T., Jones, R.H., 2009. Cooling rates of porphyritic olivine chondrules in the Semarkona (LL3.00) ordinary chondrite: a model for diffusional equilibration of olivine during fractional crystallization. *Meteorit. Planet.* Sci. 44 (4), 521–530.
Monaghan, B.J., Quested, P.N., 2001. Thermal diffusivity of iron at high temperature in both the liquid and solid states. ISIJ Int. 41 (12), 1524–1528.
Morard, G., Sanloup, C., Fiquet, G., Mezouar, M., Rey, N., Poloni, R., Beck, P., 2007. Structure of eutectic Fe–FeS melts to pressures up to 17 GPa: implications for planetary cores. Earth Planet. Sci. Lett. 263, 128–139. https://doi.org/10.1016/j.epsl.2007.09.009.
Moreau, J. (2019) Shock-darkening in ordinary chondrites: mesoscale modelling of the shock process and comparison with shock-recovery experiments. Ph.D. thesis, Unigrafia, Helsinki, 60 pp. http://hdl.handle.net/10138/300084.
Moreau, J., Kohout, T., Wünnemann, K., 2017. Shock-darkening in ordinary chondrites: determination of the pressure-temperature conditions by shock physics mesoscale modeling. Meteorit. Planet. Sci. 52, 2375–2390. https://doi.org/10.1111/maps.12935.
Moreau, J., Kohout, T., Wünnemann, K., 2018a. Melting efficiency of troilite-iron assemblages in shock-darkening: insight from numerical modeling. Phys. Earth Planet. Inter. 282, 25–38. https://doi.org/10.1016/j.pepi.2018.06.006.

Moreau J., Kohout T. and Wünnemann K. (2018b) (abstract #212) shock-darkening in a shock-recovered ordinary chondrite? Numerical model of the experiment. *2018 Eur. Planet. Sci. Congress*, Berlin, Germany, vol. 12.

Moreau, J., Kohout, T., Wünnemann, K., Halodova, P., Haloda, J., 2019a. Shock physics mesoscale modeling of shock stage 5 and 6 in ordinary and enstatite chondrites. Icarus 332, 50–65. https://doi.org/10.1016/j.icarus.2019.06.004.

Moreau J., Kohout T., Wünnemann K., Halodova P. and Haloda J. (2019b) *Shock physics mesoscale modeling of shock stage 5 and 6 in ordinary and enstatite chondrites: modeling data*, v1. doi:https://doi.org/10.5281/zenodo.2649931.

Ohno, A., 1987. Solidification: The Separation Theory and its Practical Applications. Springer-Verlag, Berlin Heidelberg, Germany, p. 123.

Osako, M., Ito, E., Yoneda, A., 2004. Simultaneous measurements of thermal conductivity and thermal diffusivity for garnet and olivine under high pressure. Phys. Earth Planet. Inter. 143–144, 311–320. https://doi.org/10.1016/j.pepi.2003.10.010.

Praprotnik, M., Šterk, M., Trobec, R., 2004. Inhomogeneous heat-conduction problems solved by a new explicit finite difference scheme. Int. J. Pure Appl. Math. 13 (3), 275–291.

Rubin, A.E., 1992. A shock-metamorphic model for silicate darkening and compositionally variable plagioclase in CK and ordinary chondrites. Geochim. Cosmochim. Acta 56, 1705–1714. https://doi.org/10.1016/0016-7037(92)90236-C.

Rubin, A.E., Scott, E.R.D., Keil, K., 1997. Shock metamorphism of enstatite chondrites. Geochim. Cosmochim. Acta 61, 847–858. https://doi.org/10.1016/S0016-7037(96)00364-X.

Sasso, M.R., Macke, R.J., Boesenberg, J.S., Britt, D.T., Rivers, M.L., Ebel, D.S., Friedrich, J.M., 2009. Incompletely compacted equilibrated ordinary chondrites. Meteorit. Planet. Sci. 44 (11), 1743–1753. https://doi.org/10.1111/j.1945-5100.2009.tb01204.x.

Schmitt, R.T., 2000. Shock experiments with the H6 chondrites Kernouvé: pressure calibration of microscopic shock effects. Meteorit. Planet. Sci. 35, 545–560.

Schmitt, D.R., Ahrens, T.J., Svendsen, B., 1987. Shock induced melting and shear banding in single crystal NaCI. J. Appl. Phys. 63 (1), 99–106.

Shabbir, G., Maqsood, A., Majid, C.A., 2000. Thermophysical properties of consolidated porous rocks. J. Phys. D. Appl. Phys. 33, 658–661.

Sharp, T.G., Xie, Z., de Carli, P.S., Hu, J., 2015. A large shock vein in L chondrite Roosevelt County 106: evidence for a long-duration shock pulse on the L chondrite parent body. Meteorit. Planet. Sci. 50 (11), 1941–1953. https://doi.org/10.1111/maps.12557.

Shaw, C.S.J., Walton, E., 2013. Thermal modeling of shock melts in Martian meteorites: implications for preserving Martian atmospheric signatures and crystallization of high-pressure minerals from shock melts. Meteorit. Planet. Sci. 48 (5), 758–770. https://doi.org/10.1111/maps.12100.

Stöffler, D. (2000), Maskelynite confirmed as diaplectic glass: indication for peak shock pressures below 45 GPa in all Martian meteorites, in: 31th Lunar Planet. Sci. Conf., abstract no. 1170.

Stöffler, D., Keil, K., Scott, E.R.D., 1991. Shock metamorphism of ordinary chondrites. Geochim. Cosmochim. Acta 55, 3845–3867. https://doi.org/10.1016/0016-7037(91)90078-J.

Stöffler, D., Hamann, C., Metzler, K., 2018. Shock metamorphism of planetary silicate rocks and sediments: proposal for an updated classification system. Meteorit. Planet. Sci. 53, 5–49. https://doi.org/10.1111/maps.12912.

Tomkins, A.G., 2009. What metal-troilite textures can tell us about post-impact metamorphism in chondrite meteorites. Meteorit. Planet. Sci. 44, 1133–1149. https://doi.org/10.1111/j.1945-5100.2009.tb01213.x.

Tomkins, A.G., Weinberg, R.F., Schaefer, B.F., Langendam, A., 2013. Disequilibrium melting and melt migration driven by impacts: implications for rapid planetesimal core formation. Geochim. Cosmochim. Acta 100, 41–59. https://doi.org/10.1016/j.gca.2012.09.044.

van der Bogert, C.H., Schultz, P.H., Spray, J.G., 2003. Impact-induced frictional melting in ordinary chondrites: a mechanism for deformation, darkening, and vein formation. Meteorit. Planet. Sci. 38, 1521–1531. https://doi.org/10.1111/j.1945-5100.2003.tb00255.x.

Wang, B., Miao, B., Wang, J., Zhang, J., 2011. Shock effects and the classification of H-chondrites from the Grove Mountains. East Antarctica: Implications for the shock history of H-chondrite parent bodies. *Adv. Polar Sci.* 22, 81–91. https://doi.org/10.3724/SP.J.1085.2011.00081.

Weinberg, M.C., Uhlmann, D.R., Zanotto, E.D., 1989. "Nose method" of calculating critical cooling rates for glass formation. J. Am. Ceram. Soc. 72 (11), 2054–2058. https://doi.org/10.1111/j.1151-2916.1989.tb06030.x.

Williams, Q., Jeanloz, R., 1990. Melting relations in the iron-sulfur system at ultra-high pressures: implications for the thermal state of the earth. J. Geophys. Res. 95 (B12), 19299–19310.

Wünnemann, K., Collins, G.S., Melosh, H.J., 2006. A strain-based porosity model for use in hydrocode simulations of impacts and implications for transient crater growth in porous targets. Icarus 180, 514–527. https://doi.org/10.1016/j.icarus.2005.10.013.

Yamaguchi, A., Sekine, T., 2000. Monomineralic mobilization of plagioclase by shock: an experimental study. Earth Planet. Sci. Lett. 175, 289–296. https://doi.org/10.1016/S0012-821X(99)00299-X.

Yomogida, K., Matsui, T., 1983. Physical properties of ordinary chondrites. J. Geophys. Res. 88 (B11), 9513–9533.

Zhang, L., Fei, Y., 2008. Effect of Ni on Fe-FeS phase relations at high pressure and high temperature. Earth Planet. Sci. Lett. 268, 212–218. https://doi.org/10.1016/j.epsl.2008.01.028.